

THESIS FOR THE DEGREE OF DOCTOR OF PHILOSOPHY IN THERMO AND AND FLUID  
DYNAMICS

# Ultra-High Pressure Spray for Gasoline Direct Injection Engines

AKICHIKA YAMAGUCHI



Department of Mechanics and Maritime Sciences  
CHALMERS UNIVERSITY OF TECHNOLOGY  
Göteborg, Sweden 2022

Ultra-High Pressure Spray for Gasoline Direct Injection Engines  
AKICHIKA YAMAGUCHI  
ISBN 978-91-7905-640-7

© AKICHIKA YAMAGUCHI, 2022.

Doktorsavhandlingar vid Chalmers tekniska högskola  
Ny serie nr 5106  
ISSN 0346-718X

Department of Mechanics and Maritime Sciences  
Chalmers University of Technology  
SE-412 96 Göteborg, Sweden  
Telephone + 46 (0) 31 - 772 1000

Typeset by the author using L<sup>A</sup>T<sub>E</sub>X.

Printed by Chalmers Reproservice  
Göteborg, Sweden 2022

# Abstract

There is an increasingly urgent need for vehicle manufacturers to reduce emissions from passenger vehicles to protect the environment and comply with increasingly stringent emissions standards such as Euro 6d, which came into force in January 2021, and Euro 7, which will probably come into force around 2025. Current emissions standards limit passenger vehicles' particulate number emissions to at most  $6 \times 10^{11}$  [# / km], making it necessary to find ways of reducing the engine-out particulate emissions of gasoline direct injection engines to meet this requirement. A promising way of doing this is to use fuel injection pressures above 200 bar, which was the most commonly used injection pressure until recently. This thesis presents a comprehensive experimental evaluation of the potential for reducing particulate number emissions from GDI engines by using high fuel injection pressures.

Basic spray characteristics such as spray tip penetration, droplet size, and spray-induced air motion were investigated in a constant-volume spray chamber. Spray tip penetration was determined by post-processing images captured with a high speed video camera, while droplet size was measured by Phase Doppler Interferometry and the motion of air around the spray was captured by means of Particle Image Velocimetry using tracer particles and a CCD camera. In addition, the behavior of combusting sprays inside a cylinder was studied using a single cylinder optical engine with a high speed video camera, and the effects of the fuel injection pressure on combustion characteristics and emissions were investigated using a single cylinder metal engine.

Increasing the injection pressure increased the spray velocity and therefore increased spray tip penetration. However, raising the injection pressure from 200 bar to 1500 bar also reduced the droplet size by over 50 % because high injection pressures enhance droplet atomization. The high spray velocities and small droplet diameters seen with an injection pressure of 1500 bar increased air entrainment into the spray: the mass of air entrained at 1500 bar injection pressure was 40% higher than at 200 bar. In addition, air entrainment occurred in a shorter time frame at higher injection pressures, which improved fuel-air mixing in the cylinder. Engine tests revealed that the use of high injection pressures reduced PN emissions by up to 50 % at standard SOI timings, and by a factor of 1000 when using advanced SOI timings under hot-steady conditions. Interestingly, the most significant effects on spray characteristics were seen when raising the injection pressure from 200 bar to 600 bar, and only relatively minor changes in spray behavior were seen when raising the injection pressure further. However, beneficial effects on emissions continued to be observed even when increasing the injection pressure to above 1000 bar.

---

**Keywords:** gasoline direct injection engine, GDI, high pressure spray, gasoline spray, particulate emission.

# List of Publications

This thesis is based on the following appended papers:

- Paper I.** Akichika Yamaguchi, Lucien Koopmans, Ayolt Helmantel, Fabian Peng Kärholm and Petter Dahlander. *Spray Characterization of Gasoline Direct Injection Sprays Under Fuel Injection Pressures up to 150 MPa with Different Nozzle Geometries*. SAE Technical Paper 2019-01-0063, SAE Powertrains, Fuels and Lubricants Meeting, San Antonio, 2019.
- Paper II.** Akichika Yamaguchi, Lucien Koopmans, Ayolt Helmantel, Johan Dillner and Petter Dahlander. *Air Motion Induced by Ultra-High Injection Pressure Sprays for Gasoline Direct Injection Engines*. SAE International Journal of Fuels and Lubricants, 13(3), 2020.
- Paper III.** Akichika Yamaguchi, Lucien Koopmans, Ayolt Helmantel, Johan Dillner and Petter Dahlander. *Spray Behaviors and Gasoline Direct Injection Engine Performance Using Ultrahigh Injection Pressures up to 1500 Bar*. SAE International Journal of Engines, 15(1), 2022.
- Paper IV.** Akichika Yamaguchi, Lucien Koopmans, Ayolt Helmantel, Johan Dillner and Petter Dahlander. *High fuel injection pressure effect on warming-up and simplified load transient conditions in gasoline direct injection engines*. Submitted to SAE International Journal of Engines.



# Acknowledgments

Throughout my PhD program, I have received a lot of support to carry out this PhD project.

First of all, I would like to thank my supervisor Prof. Petter Dahlander for his support throughout the project. He has always been kind to answer my questions and give me useful advice. I really enjoyed waling into his office and talking about my research and personal life.

I would also like to thank my co-supervisor Prof. Lucien Koopmans. His critical feedback was always helpful in correcting the course of the project and improving the quality of the papers. I would also like to thank Prof. Ingemar Denbratt for initiating this project and for his continuous support. Without this project, I would not have been able to gain such a valuable experience.

I would appreciate the support of the project members, Prof. Michael Oevermann, Ayolt Helmantel, Johan Dillner, Fabian Karrholm and Sandip Wadekar. Without their help, this project would not have been completed. In addition, I thank Martin Eriksson for his experimental support in Volvo Cars. I should thank the lab engineers at CTH for their experimental assistance. It is definitely thanks to them that I was able to complete all the experiments successfully without any serious accidents. I enjoyed working in the lab listening to their jokes.

Special thanks to my best colleagues at CaPS. They welcomed me with open arms and made my time in Sweden enjoyable. I will never forget the times we spent together wondering where to have lunch every day, and the fun times we had at Student Union after work.

Thanks also to Elenor for her administrative support. I could not have updated my residence permit without her help.

Finally, I would like to thank my parents, brothers and wife for their support and understanding of my decision to work in Sweden.





# List of Acronyms

aTDC	–	after Top Dead Center
bTDC	–	before Top Dead Center
CAD	–	Crank Angle Degree
CCD	–	Charge-Coupled Device
CFD	–	Computational Fluid Dynamics
CoV	–	Coefficient of Variation
CTH	–	Chalmers Tekniska Högskola
EU	–	European Union
EOI	–	End of Injection
GDI	–	Gasoline Direct Injection
GPF	–	Gasoline Particulate Filter
HC	–	Hydrocarbon
IMEP	–	Indicated Mean Effective Pressure
L/D	–	Length/Depth
MBT	–	Maximum Break Torque
MFB	–	Mass Fraction Burned
NO <sub>x</sub>	–	Nitrogen Oxides
PAHs	–	Polycyclic Aromatic Hydrocarbons
PDI	–	Phase Doppler Interferometry
PFI	–	Port Fuel Injection
PIV	–	Particle Image Velocimetry
PN	–	Particle Number
RDE	–	Real Driving Emissions
RON	–	Research Octane Number
SCE	–	Single Cylinder Engine
SI	–	Spark Ignition
SMD	–	Sauter Mean Diameter
SOI	–	Start of Injection
VPR	–	Volatile Particle Remover



# Contents

Abstract	iii
List of Publications	v
Acknowledgments	vii
List of Acronyms	ix
<b>I</b>	<b>1</b>
<b>1</b>	<b>3</b>
1.1	3
1.2	7
<b>2</b>	<b>9</b>
2.1	9
2.1.1	9
2.1.2	10
2.1.3	13
2.1.4	13
2.1.5	14
2.2	15
2.3	17
2.4	19
<b>3</b>	<b>21</b>
3.1	22
3.2	24
3.3	24
3.4	26
3.5	28
3.6	31
3.7	34
3.8	35
3.8.1	36

---

3.8.2	Procedure for warm-up tests . . . . .	39
3.8.3	Procedure for simplified transient tests . . . . .	39
<b>4</b>	<b>Summary of publications</b>	<b>43</b>
4.1	Paper I . . . . .	43
4.2	Paper II . . . . .	44
4.3	Paper III . . . . .	44
4.4	Paper IV . . . . .	45
<b>5</b>	<b>Results and Discussion</b>	<b>47</b>
5.1	Spray test . . . . .	47
5.1.1	Spray tip penetration . . . . .	47
5.1.2	Droplet size . . . . .	48
5.1.3	Spray-induced air motion . . . . .	50
5.2	Optical engine results . . . . .	51
5.3	Metal engine results . . . . .	53
5.3.1	Hot conditions . . . . .	54
5.3.2	Warm-up condition . . . . .	55
5.3.3	Simplified load transient conditions . . . . .	58
<b>6</b>	<b>Conclusions and Outlook</b>	<b>61</b>
	<b>Bibliography</b>	<b>65</b>
<b>II</b>	<b>Appended Papers</b>	<b>71</b>

# Part I

## Introductory chapters



# Chapter 1

## Introduction

### 1.1 Motivation

Technological development has enhanced quality of life and changed our lifestyles dramatically. However, while it is hard to imagine life without modern technologies such as electricity, phones, and transportation, our heavy use of these technologies has caused global power consumption to increase steadily over time (see Figure 1.1) [24]. Partly as a result, we are facing a range of environmental problems including climate change and pollution that are due in part to our ever-growing energy consumption.

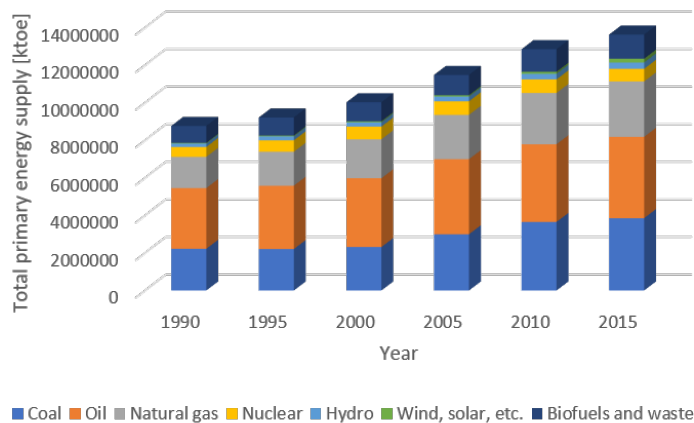


Figure 1.1: Total primary energy supply by source, World 1990-2015 [24].

Many of the transportation technologies that we use on a daily basis rely on the combustion of fossil fuels. This has a significant environmental impact, contributing to climate change. Overall, the transportation sector accounts for around 30 % of the world's total energy consumption, as shown in Figure 1.2 [16]. Consequently, there is an urgent need to reduce its environmental impact. Furthermore, the effects of exhaust gas on the human body cannot be ignored. For example, it has been reported that particulate matter such as that found in exhaust gas increases the risk of adverse heart and lung events and diseases including nonfatal heart attacks,

irregular heartbeat, aggravated asthma, and decreased lung function. [1, 10, 11, 17, 29, 39].

The automotive industry has sought to address this need by introducing new systems such as hybrid systems for gasoline-powered vehicles and common-rail systems for diesel vehicles. Governments have spurred this process by introducing strict regulations such as the EU’s EURO 6d regulations of 2020 (see Table 1.1) [13]. This process will continue; more stringent standards will come into force in the coming years (see Figure 1.3) [23]. These standards typically impose limits on CO<sub>2</sub> and particulate emissions, the reduction of which is a major challenge for both governments and the automotive industry.

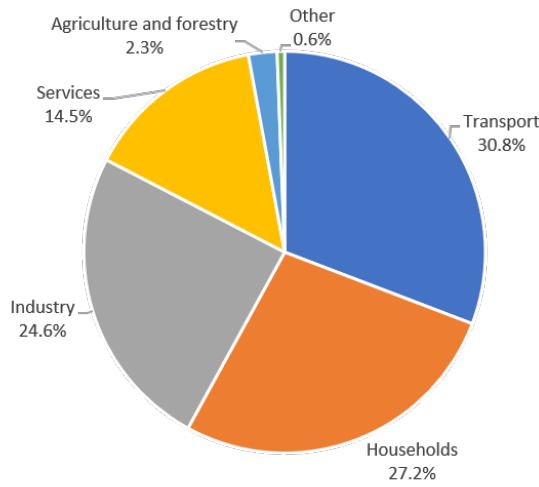


Figure 1.2: Energy consumption by sector across the EU-28 in 2017 [16]

Table 1.1: Emission standards introduced after Euro 4 for gasoline-fueled passenger vehicles [13].

Stage	Date	Cycle	CO	THC	NMHC	NOx	PM	PN [#/ <i>km</i> ]
Euro 5	2009	NEDC	1.0	0.10	0.068	0.060	0.005	-
Euro 6b	2014	NEDC	1.0	0.10	0.068	0.060	0.005	$6.0 \times 10^{11}$
Euro 6d Temp	2017	WLTC (RDE)	1.0	0.10	0.068	0.060	0.005	$6.0 \times 10^{11}$ ( $9.0 \times 10^{11}$ )
Euro 6d	2020	WLTC (RDE)	1.0	0.10	0.068	0.060	0.005	$6.0 \times 10^{11}$ ( $9.0 \times 10^{11}$ )

There is great interest in electrification of cars among automotive manufacturers because electric vehicles produce zero emissions. However, the usefulness of full electric vehicles continues to be limited by factors such as low cruise distances, long charging times, high cost, and the need for rare earth metals. To overcome these challenges, hybrid vehicles with both battery electric systems and conventional internal combustion engines (ICE) are increasingly being used. The two power sources in these vehicles complement one-another and increase overall efficiency. A recent report predicts that the number of hybrid vehicles will increase markedly in the near future (see Figure 1.4 [37]): by 2030, almost half of all newly sold vehicles are expected to be either hybrid or full electric vehicles. However, non-hybrid vehicles



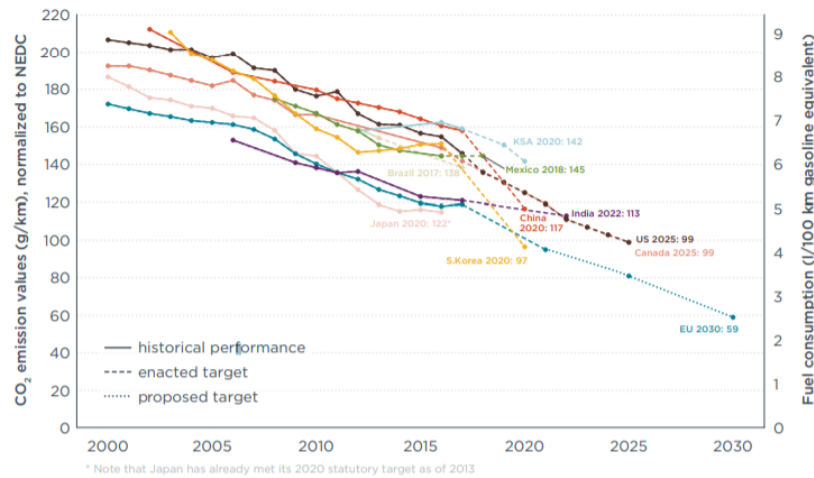


Figure 1.3: Past and future CO<sub>2</sub> emission standards[23].

with only ICE will remain abundant, and over 80 % of cars operational in 2030 will have an ICE. Therefore, the ICE will play a major role in future propulsion systems and new ICE designs with improved fuel efficiency and emissions profiles are needed to minimize adverse environmental and human health impacts.

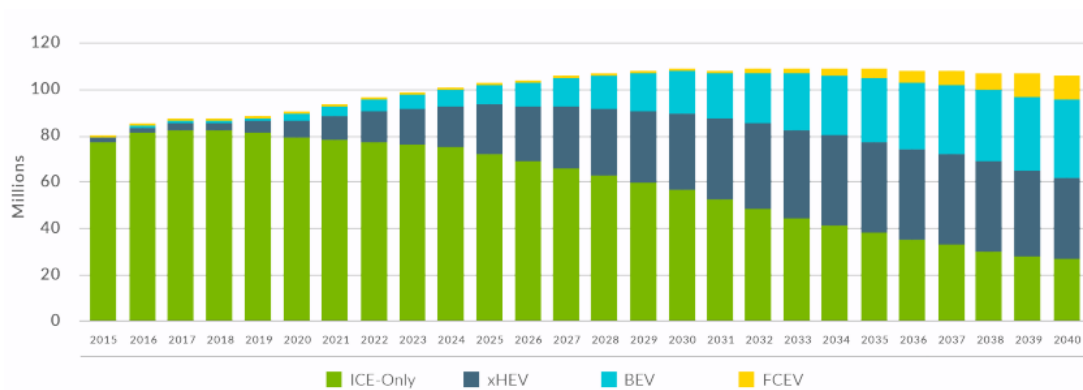


Figure 1.4: Automotive market forecasts [37]

There are two common types of ICE that use different fuel types: gasoline and diesel engines. Gasoline engines are used mainly in passenger cars whereas diesel engines are used in both light and heavy duty vehicles. Two fuel injection strategies are used in gasoline engines: Gasoline Direct Injection (GDI) and Port Fuel Injection (PFI). GDI has become increasingly popular in recent years because it offers greater fuel efficiency and a better transient response than PFI [30, 54, 67]. Fuel is injected directly into the cylinder in GDI engines whereas in PFI engines it is injected into the intake manifold. In GDI engines, fuel injection typically occurs during the intake stroke to prepare a well-mixed homogeneous mixture before ignition, so combustion proceeds under homogeneous conditions. The time available for fuel-air mixture formation in GDI engines is much shorter than in PFI engines, so GDI engines

use relatively high fuel injection pressures (around 450 bar in modern examples) to ensure that the injection process is completed quickly. The major benefits of GDI relative to PFI are:

- Lower fuel consumption due to lower pumping losses, higher compression ratios, and increased volumetric efficiency
- More precise air-fuel ratio control
- No manifold fuel film formation

GDI engines also have drawbacks relative to their PFI counterparts, namely:

- Increased particulate emissions
- Reliance on complex control and injection technologies
- Higher system costs due to high pressure fuel components
- Fuel pump losses
- Increased electrical power and voltage requirements to drive injectors and pumps

Particulate emissions are a particularly important challenge for GDI engines due to increasingly stringent regulations such as EURO 6d [13]. Finding ways to suppress these drawbacks without sacrificing any of the advantages mentioned above is therefore a key goal in GDI engine research and development. One promising approach is to simply increase the fuel injection pressure; accordingly, injection pressures in production GDI engines have risen steadily over time. The first production GDI engines used fuel injection pressures around 100 bar, but 200 bar systems are now commonplace. More recently, some companies have started introducing systems with much higher injection pressures of up to 450 bar [8, 45]. Moreover, researchers have examined the effects of using injection pressures of 600 bar and above [9, 28, 33, 38, 41, 42, 46, 47, 50, 52, 57, 58]. Increasing the injection pressure has the following consequences:

- Increased spray velocity, leading to longer spray penetration at any given timing after SOI.
- Reduced droplet sizes; significant changes in droplet size occur in the relatively low pressure range of 200 bar to 400 bar.
- Reduced particulate emissions, although the magnitude of the reduction is highly sensitive to the injection timing because of spray impingement on the piston.

While the above findings are important, some outstanding issues warrant further investigation. For example, while a number of studies have examined injection pressures of up to around 600 bar, few have examined pressures above 1000 bar. Moreover, most studies that have examined such high injection pressures examined only a limited range of test conditions.

There is thus a need for more information on spray behaviors and engine performances when using injection pressures above 1000 bar, and for a deeper understanding of the relationship between injection pressure, spray behavior, and combustion outcomes.

## 1.2 Objectives

Gasoline direct injection has been shown to have positive effects on both fuel consumption and emissions. Current commercial GDI engines use injection pressures of up to 450 bar, and previous studies on ultra-high pressure sprays have focused on diesel and GDI sprays formed at injection pressures of up to 600 bar. However, the effects of ultra-high injection pressures above 600 bar on spray characteristics and GDI engine performance have received little attention. The research presented in this thesis therefore aimed to address this knowledge gap by answering the following research questions:

- Are the beneficial effects of high injection pressures subject to saturation?  
Raising the injection pressure up to at least 600 bar is known to have favorable effects on droplet size and particulate emissions, but it is not yet clear whether further improvements can be achieved by using pressures of 1000 bar or more. If there is a saturation point for the injection pressure, it can be concluded that the injection pressure should be around the saturation point and there would be little value in using ultra-high injection pressures such as 2000 bar.
- What is the maximum achievable PN reduction factor?  
Particulate emissions are normally generated from liquid fuel in wall films or mixtures. High pressure sprays exhibit better atomization and induce more turbulence than lower pressure sprays, but it is not clear which of these effects has the greater impact on particulate emissions.
- How do ultra-high injection pressures affect other emissions and engine performance?  
While particulate emissions are particularly important because they are regulated by emissions standards, it is also important to determine how the use of ultra-high injection pressures affects emissions of other pollutants such as unburnt hydrocarbon and NO<sub>x</sub> and engine performance, which can be measured in terms of variables such as combustion stability and flame speed. If ultra-high injection pressures adversely affect other emissions or performance, it may be best to use high pressure systems only under certain conditions or in combination with other technologies such as hybrid powertrains.

The effects of ultra-high injection pressures of up to 1500 bar on spray and combustion properties were investigated by performing spray characterization experiments and single cylinder engine tests. To enable these experiments, ground-breaking custom prototype ultra-high pressure injectors were manufactured for use in this work. No injectors compatible with such high pressures existed when the project was initiated, so it was not previously possible to study the effects of such high injection pressures. Therefore, this work is not merely a study on the effects of varying parameters of existing technology; rather, it is a leading-edge investigation into the potential of ultra-high pressure systems.

The spray characterization data generated during this project will be useful in spray modeling and for improving our understanding of the physical factors responsible for the changes in spray properties observed at ultra-high injection pressures. In addition, this thesis presents new experimental data on combustion and emissions of particulates, unburnt hydrocarbon, and NO<sub>x</sub> from engines operating with ultra-high fuel pressures. This is important because spray data alone is insufficient to predict emissions. Finally, the experimental data on spray behavior and engine performance when using ultra-high injection pressures will be of interest to industrial research and development teams because the injection pressures used in production GDI engines continue to increase; the results presented herein offer insights into what kinds of fuel pressures may be used in future engines.

# Chapter 2

## Introduction to spray characteristics and GDI engines

This chapter introduces the basic characteristics of fuel sprays and engines as well as various technologies for reducing PN emissions.

### 2.1 Spray characteristics in GDI engines

Figure 2.1 depicts some of the most important physical processes that occur as a fuel spray develops in a cylinder of a GDI engine, namely fuel-air mixture formation, turbulence, and the formation of fuel films (wetting) on the piston and the liner. All of these processes are affected by the spray's properties and in turn influence the engine's combustion behavior and emissions. Another important physical process affected by spray properties is atomization, i.e. the break up of large fuel droplets into smaller ones. Atomization is important because smaller droplets evaporate more rapidly and thus improve mixture formation. Film formation depends on spray properties such as the spray direction and spray tip penetration, which must therefore be tightly controlled. Atomization can be improved by increasing the fuel injection pressure, and spray behavior can be adjusted by optimizing the design of the nozzles through which the fuel is injected. Efficient operation of GDI engines while minimizing emissions thus requires tight control over spray properties and these physical processes, which can be achieved by precisely controlling the mass of injected fuel and ensuring that the injected fuel is atomized as quickly as possible without forming fuel films on engine components.

#### 2.1.1 Injector type and spray shape

There are three main nozzle types used in GDI engines: multi-hole, outward-opening, and swirl nozzles. Figure 2.2 shows the structural differences between these nozzle types and the different spray shapes they produce [64]. The nozzle needle moves inwards in both multi-hole and swirl nozzles, but these two nozzle types produce rather different spray shapes. Multi-hole nozzles create multiple spray plumes that develop more or less in alignment with the nozzle hole axis. Conversely, swirl nozzles

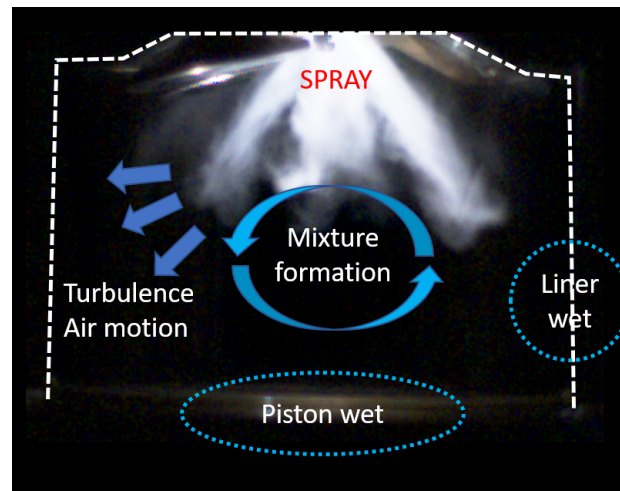


Figure 2.1: Key physical processes affected by spray behavior in the combustion chamber.

create hollow cone-shaped sprays because of swirl flow inside the nozzle. Like swirl nozzles, outward-opening nozzles also create hollow cone sprays. However, the shape of these sprays differs from those emitted by swirl nozzles because of differences in the internal nozzle flow and spray development (see Figure 2.3) [56]. The advantages and drawbacks of these three nozzle types are shown in Figure 2.4 [51]. Swirl nozzles have a number of benefits but these are most pronounced at relatively low injection pressures (around 100 bar). Significantly different outcomes may be observed at higher injection pressures ( $> 400$  bar) because high pressure sprays exhibit improved atomization and greater robustness against fouling.

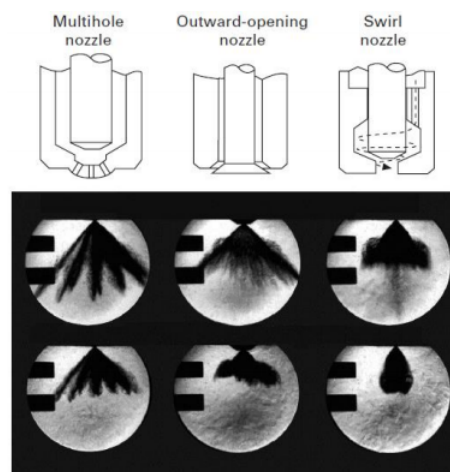


Figure 2.2: Differences between nozzle shapes and the sprays they produce [64]

### 2.1.2 Atomization

The conversion of pressurized fuel into a combustible fuel-air mixture is a key process during fuel injection. Atomization plays a key role in mixture formation because

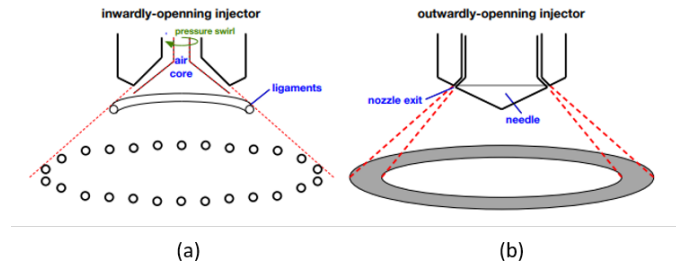


Figure 2.3: Schematic depictions of hollow-cone sprays and film structures. (a) Swirl nozzle. (b) Outward-opening nozzle [56].

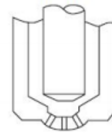

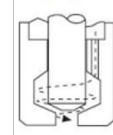
Nozzle type	Multihole nozzle	Outward-opening nozzle	Swirl nozzle
Structurew			
Flexibility of spray pattern	++	+	+
Potential for inclined of spray axis	+	-	++
Atomization quality at 100 bar	-	0	++
Robustness against fouling	-	++	+

Figure 2.4: Properties of the three nozzle designs [51].

it is the process whereby the bulk liquid fuel is converted into small droplets that evaporate readily. It occurs in two stages that are known as primary and secondary break-up (see Figure 2.5)[3]. Primary break-up is dominated by the cavitation in the nozzle flow and generates large ligaments and droplets that form a dense spray near the nozzle. Cavitation is influenced by the injection pressure, nozzle hole geometry, and the properties of the fuel and surrounding medium. Secondary break-up is driven by disruption of consolidating forces, particularly the surface tension of the liquid fuel. The surface tension of a liquid depends strongly on its viscosity and tends to cause liquid droplets to adopt spherical shapes to minimize their surface area to volume ratio. Aerodynamic forces counteract the consolidating effect of surface tension and thus favor droplet break-up.

### Primary break-up

Primary break-up can occur via several modes, as shown in Figure 2.6. *Rayleigh breakup* is caused by surface tension-induced growth of axisymmetric oscillations of the jet surface. The resulting drop diameters are comparable to the nozzle diameter. *First wind-induced breakup* is caused by an increase in surface tension due to the velocity of the jet relative to that of the ambient gas. This creates a static pressure distribution across the jet, accelerating the breakup process. The resulting drop sizes are generally similar to the jet diameter. *Second wind-induced breakup* is caused by the unstable growth of short-wavelength surface waves on the jet surface and generates droplets whose average diameter is smaller than the jet diameter. This

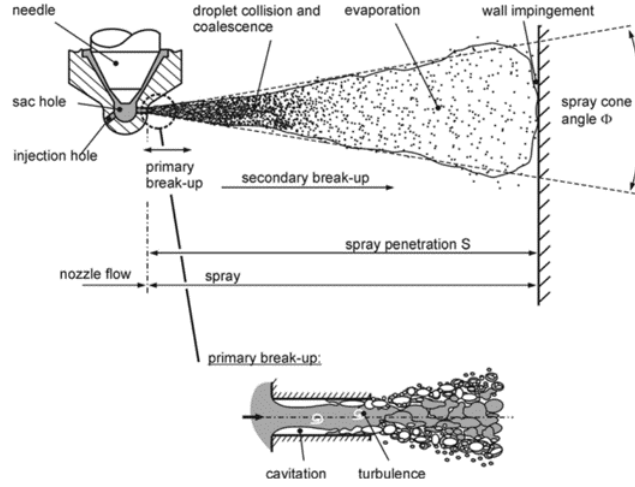


Figure 2.5: Break-up of a full-cone diesel spray [3]

wave growth is opposed by surface tension. Finally, in the *atomization* regime, the jet is disrupted completely at the nozzle exit. Average droplet diameters are thus much smaller than the jet diameter. The relative contributions of these modes depend heavily on three dimensionless parameters: the Weber, Reynolds, and Ohnesorge numbers [34]. The Weber number describes the ratio of the inertial forces to the surface tension and is defined by equation 2.1; it depends on the relative velocity  $v$ , density of the liquid  $\rho_l$ , nozzle hole diameter  $D$ , and surface tension  $\sigma$ .

$$We_l = \frac{v^2 D \rho_l}{\sigma} \quad (2.1)$$

The Reynolds number describes the relationship between the internal forces and the viscous force of fluid flow, and is computed using equation 2.2. The contributions of the internal forces depend on the liquid velocity  $v$ , the density of the liquid  $\rho_l$ , and the nozzle hole diameter  $D$ , while the contribution of the viscous forces depends on the dynamic viscosity of the liquid  $\mu_l$ .

$$Re = \frac{v D \rho_l}{\mu_l} \quad (2.2)$$

By eliminating the jet velocity  $v$ , Ohnesorge derived the dimensionless Ohnesorge number, which depends on key fluid properties (the dynamic viscosity  $\mu_l$ , the surface tension  $\sigma$ , and the density of the liquid  $\rho_l$ ) and the nozzle hole diameter  $D$  [43].

$$Oh = \frac{\sqrt{We}}{Re} = \frac{\mu_l}{\sqrt{\sigma \rho_l D}} \quad (2.3)$$

### Secondary breakup

Secondary breakup occurs after primary breakup. Its progression depends on the balance between the consolidation force acting on the droplet and the disruption force. The consolidation force acts to preserve the droplet's shape, whereas the disruption



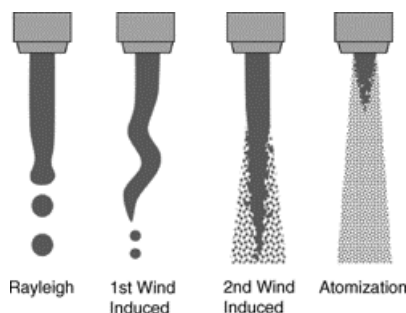


Figure 2.6: Typical breakup regime for a plain-orifice liquid injection nozzle [34]

force is drag caused by the velocity of the droplet relative to the ambient gas. If the disruption force is stronger than the consolidation force, the droplet breaks up into smaller droplets. The balance between these forces is described by Equation 2.4, where the left-hand term represents the consolidation force and the right-hand term represents the disruption force.  $D$  is the droplet diameter,  $\sigma$  is the surface tension,  $U_R$  is the relative velocity between the droplet and the ambient gas, and  $C_D$  is the drag coefficient. Surface tension is main determinant of the consolidation force, and the relative velocity, droplet diameter, and gas density are the main determinants of the disruption force.

$$\pi D \sigma = \frac{1}{2} \rho_a U_R^2 C_D \frac{\pi D^2}{4} \quad (2.4)$$

It should be noted that the above equation only describes the breakup of a single droplet. Actual breakup processes in real sprays are more complex because phenomena such as breakups, collisions, and recoupling occur simultaneously.

### 2.1.3 Spray Penetration

The spray penetration is the length of the liquid-phase spray plume from the nozzle tip (see Figure 2.5). It strongly affects spray characteristics and behaviors because the liquid spray will impinge on the piston/liner if the penetration is too high. The development of a typical diesel spray is shown in Figure 2.7 [59]. The spray tip penetration depends on the relative magnitudes of two opposing forces: (1) the kinetic energy of the initial liquid jet and (2) the aerodynamic resistance of the surrounding gas. The initial jet velocity is usually high, but as atomization proceeds and the spray's surface area increases, the kinetic energy of the liquid is gradually dissipated by frictional losses to the gas. When the drops have finally exhausted their kinetic energy, their subsequent trajectory is dictated mainly by gravity and/or the movement of the surrounding gas.

### 2.1.4 Droplet Size Distribution

The droplet size distribution describes the size of the droplets comprising the spray. A typical size distribution is shown in Figure 2.8 [35]. Size distribution curves are typically either number- or volume-based. Volume-based size distributions are

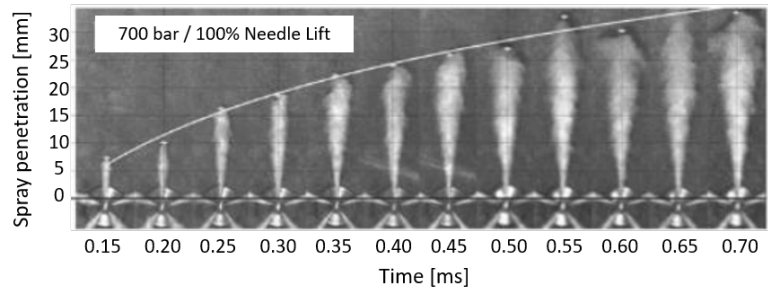


Figure 2.7: Spray dispersion over time [59]

weighted towards larger droplets, so the resulting graphs are right-skewed compared to the corresponding number-based size distributions (see Figure 2.9 [35]). GDI sprays generally have an arithmetic mean diameter of 10 to 20  $\mu\text{m}$ , whereas PFI sprays generally have a much larger mean diameter of around 100  $\mu\text{m}$ . Generally, small droplets vaporize quickly whereas large droplets vaporize slowly. Increasing the injection pressure improves atomization, reducing the size of the droplets in the spray and shifting the peak of the size distribution curve to the left. This is important because it reduces the abundance of large droplets and thus reduces the total vaporization time.

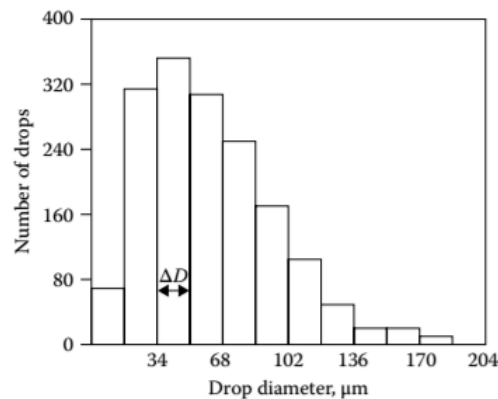


Figure 2.8: A typical droplet size distribution [35].

### 2.1.5 Spray-induced air motion

Spray-induced air motion can have important effects on mixture formation. Induced air motion is caused by exchange of momentum between the spray and the surrounding air. The extent of this exchange depends on the spray's shape, velocity, and degree of atomization. As a result, it develops in parallel with the spray itself, as shown in Figure 2.10. Shortly after the start of injection (SOI), the spray pushes the air away and the exchange of momentum between the spray and the surrounding air increases. At this stage, the air motion is not fully developed because the momentum exchange is delayed. Towards the end of the injection, the air motion becomes fully developed,

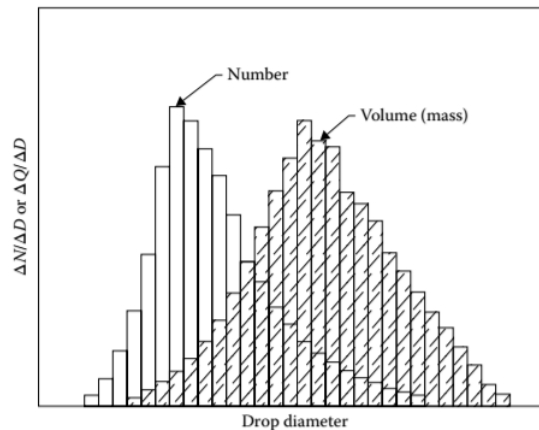


Figure 2.9: Droplet size distributions based on number and volume [35].

creating a recirculating flow from the spray tip to the upstream region of the spray. The induced air motion thus causes entrainment of air into the spray. After the end of the injection, the spray-induced air motion remains but decays gradually because there is no further input of momentum from the spray. All this air motion originates from the spray-air interaction, which thus influence atomization, mixture formation, and the overall turbulence in the cylinder.

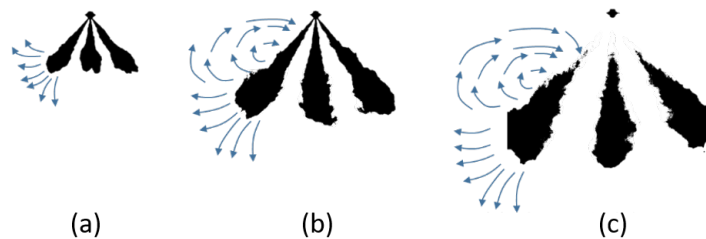


Figure 2.10: Development of the spray-induced air motion over the course of the injection: (a) the early stage of the injection, (b) during the injection, (c) after the end of the injection.

## 2.2 Particulate emissions from GDI engines

Particulate emissions are generated during both the combustion and exhaust phases of the engine cycle. The main process responsible for particle formation in the cylinder is pyrolysis, whereby fuel molecules are degraded and converted into polycyclic aromatic hydrocarbons (PAHs). The PAHs in turn give rise to small soot particles known as soot precursors, which accumulate mass and become primary soot particles that grow into larger particles via surface growth reactions. Figure 2.11 presents a schematic depiction of the soot formation process and shows the dependence of the soot output on the temperature and air-fuel ratio; the soot output is highest at temperatures of 1600-1800 K. In laminar flames, the different stages of soot formation occur in visually distinct regions of the flame. However, in the more complex turbulent flames

typically formed during premixed combustion, all of the stages occur simultaneously, in overlapping regions of space [12].

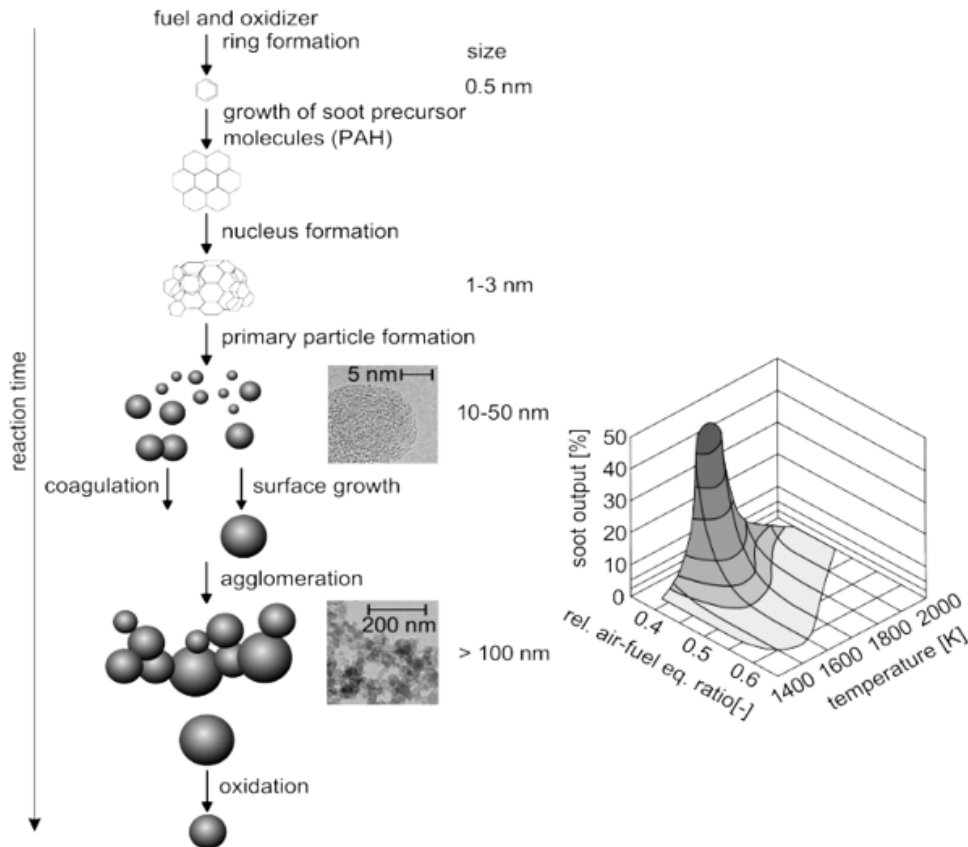


Figure 2.11: The soot formation process and the dependence of the soot output on the temperature and air-fuel ratio [5, 6, 7]

In general, soot formation depends on the local temperature and the local air-fuel ratio [6]. Fuel-rich mixtures are undesirable for homogeneous stoichiometric combustion but are often formed due to poor air-fuel mixing and impingement of sprays on the cylinder walls. Wall films resulting from spray impingement may remain on the component surface until ignition due to poor vaporization if the wall temperature is low and the time for evaporation is short. Key sites of particulate formation in the cylinder are shown in Figure 2.12 [32]. Under cold conditions, particulate emissions are mainly formed in locations coated with fuel films such as the pistons, liners, and intake valves. Under hot condition, particle formation occurs mainly at the injector tip and pistons. Because the piston is an important site of particulate formation in both cases, reducing particulate formation at the piston could substantially reduce PN emissions over a complete driving cycle.

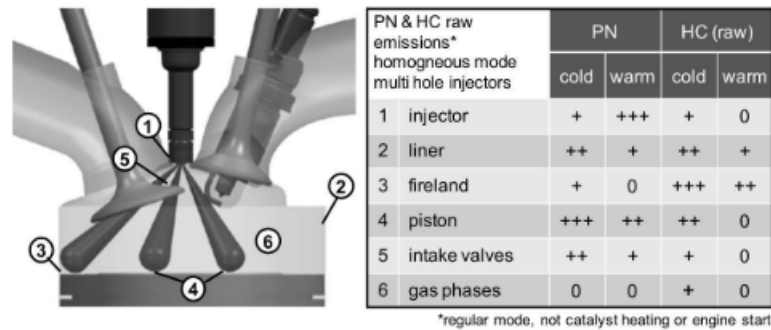


Figure 2.12: Major sources of PN and HC emissions in the cylinder [32]

## 2.3 Current techniques for reducing PN emissions

### Increasing the injection pressure

Increasing the fuel injection pressure increases air entrainment into the spray and improves atomization, making it an attractive strategy for reducing particulate emissions [65, 66]. The potential benefits of high injection pressures for GDI engines have been discussed extensively [9, 28, 33, 38, 41, 42, 46, 47, 50, 52, 57, 58], and the wide recognition of these benefits has been reflected in a gradual increase in the injection pressures used in commercial GDI engines [8, 45, 49].

High injection pressures improve fuel-air mixing and accelerate evaporation because they enhance turbulence and atomization, leading to lower PN emissions. In addition, high injection pressures have favorable effects on wall film formation, which is important because wall films are a major site of particulate formation as shown in Figure 2.12. Increasing the injection pressure tends to increase the wall film area but reduces the wall film mass [55], leading to a significant overall reduction in film thickness. Thinner films evaporate more quickly, and thus give rise to less soot. A drawback of high injection pressures is that they increase spray tip penetration due to the high initial velocity of the spray, which could cause significant spray impingement on the piston.

### Optimization of fuel injection timing

The SOI timing must be carefully optimized so as to maximize the mixing time while avoiding fuel film formation on the piston. In homogeneous combustion mode, the fuel is injected during the intake stroke, which could cause significant impingement on the piston if the SOI timing is too early. Delaying the SOI increases the distance between the injector nozzle and the piston and thus reduces wall film formation. However, if the SOI timing is too late, the mixing time before ignition may be too short, leading to incomplete air-fuel mixing. Figure 2.13 illustrates the typical dependence of PN emissions on the SOI timing: PN emissions are high at advanced SOI timing likes  $340^\circ\text{bTDC}$  due to significant piston impingement and at very late SOI timings around  $180^\circ\text{bTDC}$  due to poor mixing. Therefore, the optimal SOI timing in terms of PN emissions is in the range of  $310\text{-}270^\circ\text{bTDC}$ .

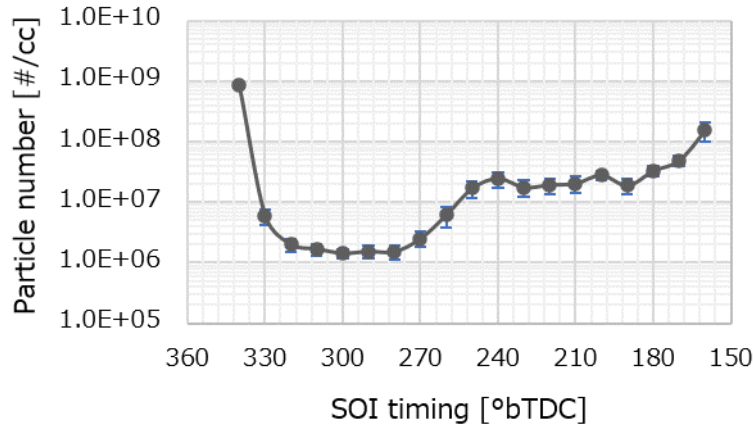


Figure 2.13: Dependence of PN emissions on the SOI timing

## Split injection and multiple injection

Multiple injection strategies divide injection events into two or more injections. The benefit of this approach is that the fuel mass in each injection is reduced, meaning that the momentum of the resulting spray, the spray tip penetration, and the impingement on the cylinder wall are also reduced. This reduces wall film formation and thus leads to lower PN emissions [19, 60, 63]. Although it has been shown that multiple injection strategies can reduce PN emissions, their optimization requires careful consideration of parameters and factors including the split ratio, injection interval, and the potential shortening of the mixing time.

## Modifying nozzle design

The design of the injector nozzle has important effects on spray properties; among other things, it influences the spray's direction and shape as well as the wetting of the injector tip. Multi-hole nozzles are generally used in GDI engines because their designs can readily be tuned to direct the spray in optimal directions. The spray direction should be chosen so as to maximize fuel-air mixing while minimizing the formation of fuel films on the cylinder walls. The spray shape strongly affects both the spray tip penetration and the spray-induced air motion; shorter and wider sprays are generally preferable in both respects. Injector tip wetting should ideally be minimized because it leads to injector fouling, i.e. the formation of deposits on the injector tip that increase PN emissions [15, 20, 25, 26, 31, 48]. Fuel deposition on the injector tip increases PN emissions for several reasons: (1) it increases spray tip penetration and thus wall film formation, (2) it reduces spray quality, leading to incomplete combustion and increased fuel leakage during injector closing, and (3) fuel absorption by porous deposits leads to the formation of a diffusion flame after the combustion period [2, 62]. The latter effect leads to the phenomenon known as injector aging or PN drift, i.e. the tendency for old used injectors to generate higher PN emissions than new clean injectors (see Figure 2.14). Tip wetting can be reduced

by using an optimized nozzle tip design, slowing the build-up of deposits [44].

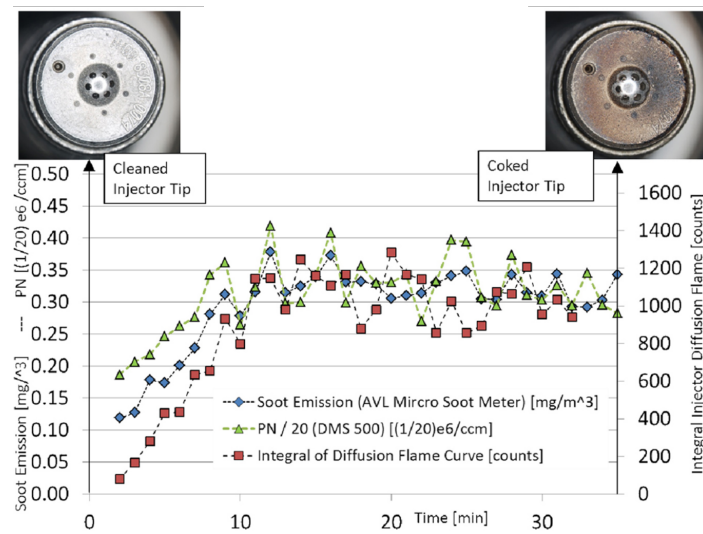


Figure 2.14: An example of PN drift caused by injector tip deposition [4]

## 2.4 Novelty of the research

To meet the challenges of climate change while complying with increasingly stringent emissions standards, future internal combustion engines will have to be designed to achieve the highest possible fuel efficiency while minimizing emissions of particulates and other pollutants. The research presented in this thesis was intended to help meet these requirements by clarifying the potential for using ultra-high fuel injection pressures to reduce particulate emissions. Previous studies have shown that the use of injection pressures around 500 bar can reduce PN emissions [52], but the effects of using even higher injection pressures are largely unknown. This work examines the effects of injection pressures as high as 1500 bar, which greatly exceed the highest fuel pressure used in any production engine (450 bar) and the fuel pressures examined in previous studies. Such ultra-high injection pressures are expected to enhance atomization and intensify turbulence while also reducing the duration of injection events. The results presented herein clarify the benefits of ultra-high injection pressures and the potential for exploiting these benefits in future internal combustion engines.

The effects of injection pressures around 1500 bar have been examined in some earlier studies. For example, Migliaccio et al. reported an experimental and numerical study on hollow cone sprays formed at high injection pressures up to 1200 bar [41]. Their experimental results showed that the penetration of these sprays was much shorter than that observed with conventional multi-hole nozzles. These findings were supported by the results of simulations using a computational fluid dynamics (CFD) spray model. Medina et al. reported an experimental study based primarily on imaging with a high speed camera in which they investigated the properties of sprays formed at fuel pressures up to 1500 bar [38]. Their results showed that the

penetration length increased with the injection pressure, as expected. In addition, it was found that the spray shape was affected more strongly by the ambient pressure than the fuel pressure. Lehnert et al. experimentally studied the spray shapes and particle size distributions obtained with nozzles designed for use with gasoline and diesel at a fuel pressure of 2000 bar [36]. These investigations showed that the relationship between penetration and injection pressure depended on the atmospheric conditions; in some cases, increasing the fuel pressure did not greatly increase the penetration length. Additionally, diesel-type nozzles were shown to promote rapid fuel evaporation at very high fuel pressures, while gasoline-type nozzles were more efficient at reducing penetration at moderate fuel pressures.

As the above discussion shows, only a handful of studies have examined injection pressures above 1500 bar and those that have been reported have focused exclusively on spray properties. The work presented herein therefore has significant novelty because it includes experimental studies on engine performance and combustion behavior when using ultra-high injection pressures in addition to characterization of spray properties.



## Chapter 3

# Experimental Setup and methods

To answer the research questions posed in the Introduction, spray characterization studies and thermal experiments were performed at ultra-high injection pressures of up to 1500 bar. Injection rates, spray tip penetration, spray break-up, droplet sizes, and air entrainment were measured using an injection rate meter, spray imaging, PDI, and PIV, respectively. Thermal experiments were performed under several conditions using a single cylinder engine (SCE). Engine tests under hot and steady conditions were performed to investigate the effect of ultra-high injection pressures on engine performance and emissions. However, as shown in Figure 3.1, the cold-start, warm-up and load transient phases are the dominant contributors to total PN emissions over a driving cycle [63]. During the cold-start and warm-up phases, the temperatures of the cylinder wall and the piston are considerably lower than during steady-state operation, so the fuel injected into the combustion chamber evaporates more slowly than under hot conditions. The non-evaporated (i.e., liquid) fuel in the mixture and the wall films causes incomplete combustion, resulting in high PN emissions. During load transient states, the mass of fuel injected increases suddenly due to a sharp increase in the required torque. This increases the formation of wall films and leads to the formation of a fuel-rich mixture, both of which tend to increase PN emissions. Therefore, additional SCE tests were performed under warm-up and simplified transient conditions using injection pressures of up to 1500 bar.

To perform these experiments, an experimental system capable of sustaining ultra-high injection pressures while exerting precise control over injections was needed. Such a system was created during the course of the work presented here. This system uses a custom-made high pressure fuel pump for spray tests and a diesel pump for engine tests to deliver injection pressures between 200 bar and 1500 bar. Consequently, the maximum injection pressure deliverable with the new system greatly exceeds both the highest injection pressure currently used in a production engine (450 bar) and the injection pressures commonly used in engine research (500 - 600 bar). Accurate control of the injection duration is achieved by using a diesel injector. However, normal diesel nozzles are inappropriate for GDI sprays and engines, so the injector was fitted with a modified nozzle designed to produce a spray shape similar to that generated by conventional GDI injectors. Details of this unique system are presented in the following section.

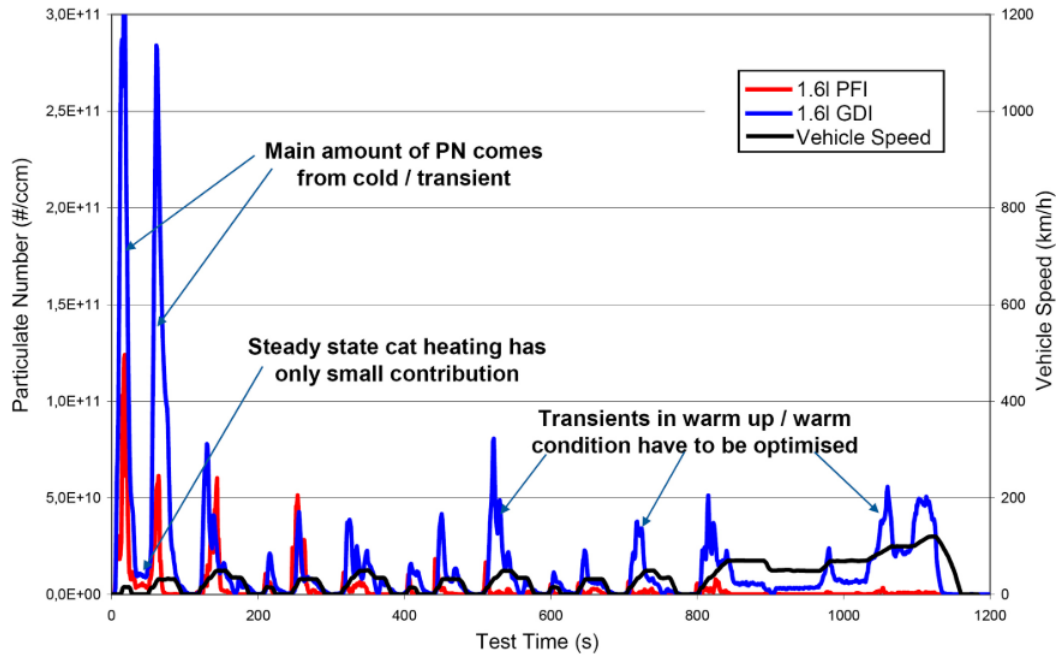


Figure 3.1: PN emissions over the NEDC cycle for PFI and GDI engines [63]

### 3.1 Injector

The injector is a key component of the fuel injection system that controls the injection mass and spray behavior at a given injection timing. The injection process is important in GDI engines because spray behavior in the cylinder strongly affects engine performance and emissions. One of the objectives of this project was to identify injector nozzle shapes that maximize the benefits achieved by using high injection pressures. To this end, experiments were conducted to determine how nozzle shape affects spray characteristics and to gather data to support the development and validation of models to be used in spray simulations. Four different injectors were used in this campaign; their specifications are listed in Table 3.1. Typical injectors for GDI engines can only handle fuel pressures of up to 350 bar, so a diesel-type injector capable of withstanding pressures of up to 1500 bar was used in the experimental system. A range of modified nozzle types were used with this injector. The injector body is based on a mass-production model manufactured by the DENSO corporation. The tested nozzles have different shapes and numbers of holes, and the ratio of the nozzle thickness to the hole diameter ( $L/D$ ) was higher than is typical for GDI injectors to enable the nozzles to withstand high injection pressures.

In this context, a divergent nozzle is one where the inlet diameter is smaller than the outlet diameter; the opposite is true for a convergent nozzle. Schematic depictions of the nozzles' hole configurations and hole arrangements are shown in Figure 3.2 and Figure 3.3. All four injectors were operated at a common flow rate chosen to be representative of the flow rate in a typical GDI injector. This required each nozzle to have a different minimum diameter.

Table 3.1: Injector specifications

	Injector #1	Injector #2	Injector #3	Injector #4
Hole shape	Divergent	Convergent	Divergent	Cylindrical
Number of holes	6	6	10	10
Mass flow rate	15 mg/ms at 200 bar			
L/D	5.45	5.56	5.34	5.47
Cone angle of hole	15	2	15	0

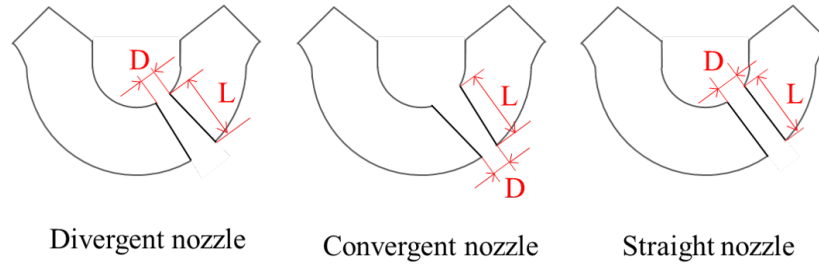


Figure 3.2: Schematic depiction of the nozzle shapes.

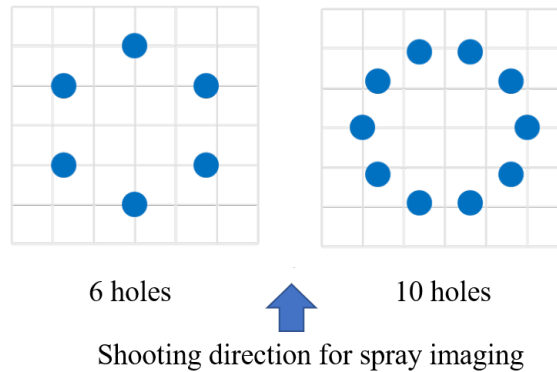


Figure 3.3: Spray targets for 6- and 10-hole injectors.

These injectors are driven by piezoelectric actuators, enabling quick and accurate control of needle movement. The opening and closing of the needle is driven by the difference in pressure between the fuel injection and the return flow; the mechanism of the needle's movement is shown in Figure 3.4 [14]. An injection event can be divided into three main stages: non-injection, injection, and after injection. During the non-injection stage, the pressure in the control chamber and in the bottom of the nozzle needle are identical to the injection pressure, so the needle is closed due to the difference in the surface areas. A voltage is applied when the injection starts, causing the piezoelectric actuator to expand. The force from the actuator is transmitted to the control valve through the large and small diameter pistons. This transmitted force causes the control valve to open, at which point fuel is discharged from the control chamber to the return flow side, reducing the pressure in the control chamber. The resulting difference in pressure between the control chamber and the bottom of the needle causes the needle to rise. When the voltage is cut off, the pistons and

the control valve in the control chamber rise, causing the lower seat to open and the upper seat to close. The pressure in the control chamber then immediately becomes equal to the injection pressure, causing the needle to be pushed down and stopping the injection.

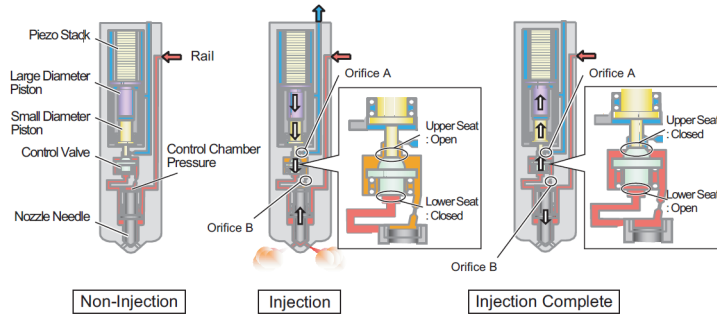


Figure 3.4: Injection mechanism [14]

## 3.2 Fuel pump

Two different fuel pumps were in the experiments presented herein: a custom-made pump for the spray tests and a diesel pump for the engine tests. The custom-made fuel pump can be used with low lubricity fuels such as n-heptane. It consists of a controller, a magnetic valve, a hydraulic oil pump, a low pressure pump, and a main high pressure piston. The hydraulic oil pump drives the main piston, while the low pressure pump feeds the fuel from the fuel tank to the piston. The volume inside the cylinder is around 100 cc. The piston pressurizes the fuel to a preset value and the regulator valve feeds the high pressure fuel to the injector. The pump exhibits high wear resistance and is less prone to pressure pulsations than conventional pumps because the fuel is pressurized by a single movement of the piston. This minimizes undesired effects on spray behavior.

For the engine tests, injection pressures above 1000 bar were generated using a diesel pump driven by a motor. Normal gasoline fuel has insufficient lubricity for use with a diesel pump, so a lubricity improver was added to avoid pump damage. The lubricant's concentration was 800 ppm and preliminary experiments indicated that its presence at this concentration had negligible effects on spray behavior (spray shape, penetration, and droplet size) and combustion behavior (stability, combustion speed, and emissions).

A common rail was installed next to the injectors for both fuel pump systems to minimize sudden pressure drops and fuel pressure pulses caused by injection events.

## 3.3 Injection rate meter

Injection rates were measured with a Loccioni Mexus 2 Zeuch-type injection rate meter (see Figure 3.5). The main purpose of performing such measurements is to understand

the injector's flow characteristics and the relationship between the injection pulse and the actual injected mass. The injection rate meter system consisted of a control chamber, a pressure sensor, a regulation valve, and a Coriolis meter. The control chamber was pre-pressurized with fuel up to a pre-defined back pressure and the effect of this back pressure on the injection rate was investigated. This feasibility test showed that higher back pressures suppressed noise in the injection rate signal, so the highest possible back pressure (25 bar) was used in this work. There was a continuous outflow due to injections and the needle of the regulation valve was adjusted automatically to maintain the specified back pressure inside the control chamber. When the injector injected fuel into the pressurized control chamber, the pressure sensor detected the resulting pressure wave. The signal of the pressure wave was then filtered and post-processed to derive the injection rate. The Coriolis meter accurately measured the injection mass and the mean mass flow, which were used to calculate the injection rate. The injectors were mounted in a custom-made injector fixture designed to ensure that the mechanical vibrations of the injector's actuator would have minimal effects on the pressure signal. The system's backpressure was set to a value significantly higher than that expected in a real engine to suppress internal cavitation in the hydraulic volume. High back pressures generally have only minor effects on the injection rate, and were found to have no significant impact in this work. The injection frequency, injection duration, chamber pressure and signal analysis were controlled by the Loccioni software. The experimental conditions applied during injection rate measurement are listed in Table 3.2.

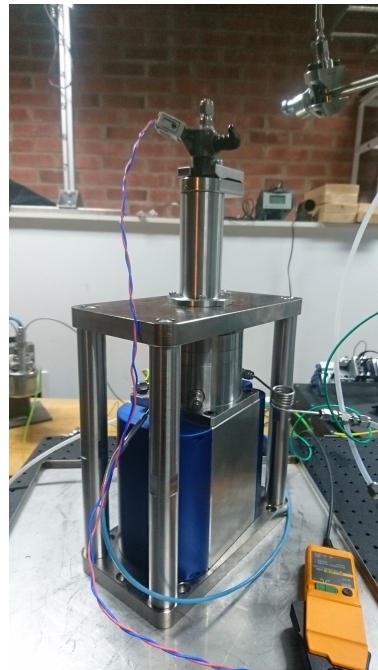


Figure 3.5: Picture of the injection rate meter.

Table 3.2: Experimental conditions for injection rate measurement.

Parameters	Units	Values
Fuel type		n-heptane
Fuel temperature	K	293
Fuel pressure	bar	200, 400, 600, 800, 1000, 1200, 1500
Control chamber temperature	K	323
Control chamber pressure	bar	25
Injection frequency	Hz	20
Number of shots	shot	200
Measuring range	mg/shot	0.4 - 150
Resolution	mg	0.01
Accuracy	mg/shot	$\pm 0.05$ (range 0 - 50 mg/shot)
	mg/shot	$\pm 0.2$ (range 0 - 150 mg/shot)

### 3.4 Spray Imaging

A high-speed video camera was used to capture shadowgraph images of liquid sprays in a constant volume chamber using a solid state plasma light for back illumination and a diffuser. Figure 3.6 shows a schematic depiction of the experimental setup. The images were post-processed and analyzed to determine spray characteristics such as the spray tip penetration and spray plume angles. The experimental conditions (including the high speed video camera settings for the spray imaging experiments) are listed in Table 3.3. Back illumination is a robust method for measuring penetration and spray plume angles because it creates a clear boundary between the liquid spray region and the surrounding air, giving a high signal to noise ratio.

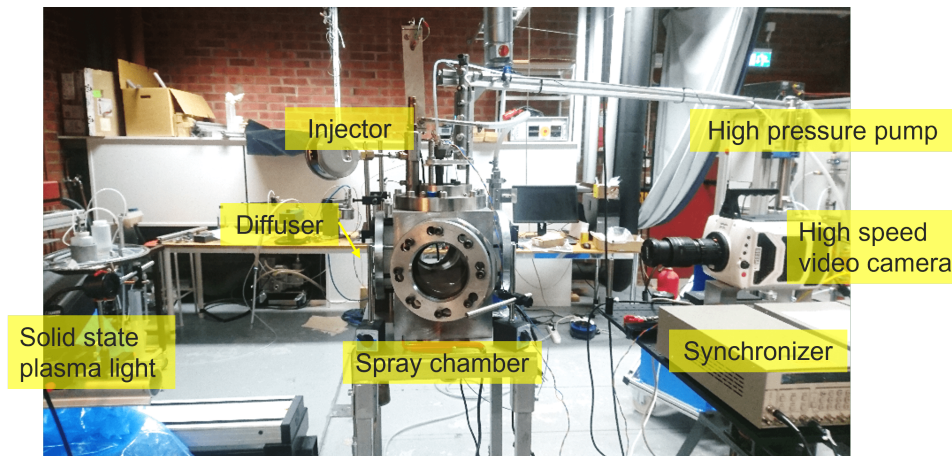


Figure 3.6: Setup of the spray imaging apparatus.

Spray images taken with the high speed video camera were post-processed in Matlab to determine the spray tip penetration length and breakup length. Captured spray images were binarized using a predefined threshold value; because the signal to noise ratio was high, the calculated spray tip penetration was relatively insensitive to the exact choice of threshold. A single spray plume was selected to calculate

Table 3.3: Experimental conditions for spray imaging.

Parameters	Units	Values
Injector		Divergent 6 hole Convergent 6 hole Divergent 10 hole Straight 10 hole
Fuel type		n-heptane
Fuel temperature	K	293
Fuel pressure	bar	200, 400, 600, 800, 1000, 1200, 1500
Injection mass	mg	27
Chamber gas		air
Chamber gas pressure	bar	1, 6
Chamber gas temperature	K	293
Frame rate	fps	19000
Image size	pixel $\times$ pixel	768 $\times$ 768
Image resolution	mm/pixel	0.1489

penetration, which was done by applying a mask. Spray tip penetration along the injector axis was determined by measuring the distance between the nozzle tip and the spray tip. However, this distance is the penetration along the injector axis, and therefore had to be rescaled to determine the penetration along the spray axis. This was done based on the camera's viewing angle and the spray direction (see Figure 3.7). The average penetration was calculated as the mean penetration of 20 images. Breakup points were determined from time-resolved spray tip penetration curves using the procedure developed by Hiroyasu and Arai [21]; a typical penetration curve is shown in Figure 3.8. The curve is plotted with a logarithmic scale, and the gradient at early timings clearly differs from that at later timings. Two lines extending these two gradients are superimposed on the plot; their point of intersection is defined as the breakup point. The breakup point is used to determine the breakup time and breakup length of the spray. If there is no clear change in gradient, the spray exhibits no detectable deceleration and the breakup point cannot be determined.

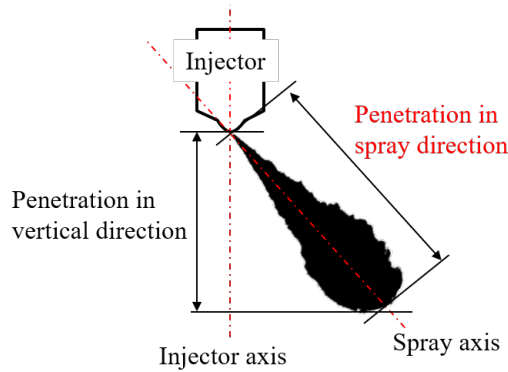


Figure 3.7: Penetration along the injector axis and the spray axis.

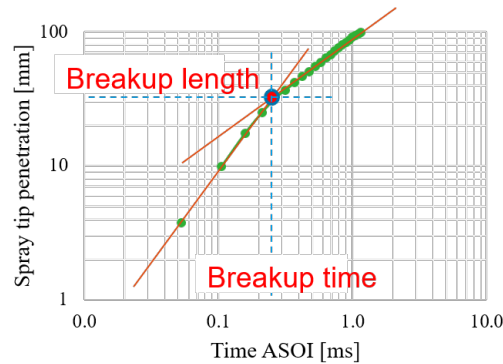


Figure 3.8: Identification of the breakup point based on a penetration curve [21].

### 3.5 Phase Doppler Interferometry

An Artium 2D Phase Doppler Interferometer (PDI) was used for droplet size measurement. The PDI system consists of a transmitter, receiver, and analyzer and is shown in Figure 3.9. The two laser beams emitted by the transmitter intersect to create a measurement volume. The interferometer was used in refractive mode to maximize signal strength and quality, and a receiver was positioned with an off-axis angle of 34 degrees to the transmitter. The PDI settings and conditions used in these experiments are listed in Table 3.4. A programmable three-axis traverse system was used to control the measurement position. The measurement position used in this work was 80 mm downstream of the injector tip and 5 mm outside the spray core. The number density of high-pressure sprays is very high (as is also the case for diesel sprays), which makes PDI measurements impossible close to the nozzle and in the center of the spray plumes. The divergent 6-hole injector was used in the PDI experiments because the droplet number density in the regions just outside the center of its spray plumes was low enough to enable reliable measurement. Even so, at the studied high injection pressures, the droplet number density became too high for measurement when the injection rate was high, greatly reducing the number of validated droplets. The measurement time window was chosen such that droplet size was only measured during the injection event. Results for a typical time window together with the corresponding pulse input and injection rate trace are shown in Figure 3.10. There is a small delay between the needle opening signal and the start of size measurement because of the delayed appearance of the liquid spray. Similarly, at the end of the measurement period, there is a delay between the closing of the needle and the end of spray ejection. The measurement time window was chosen to end when the droplet velocity fell to two-thirds of its initial value (see Figure 3.10).



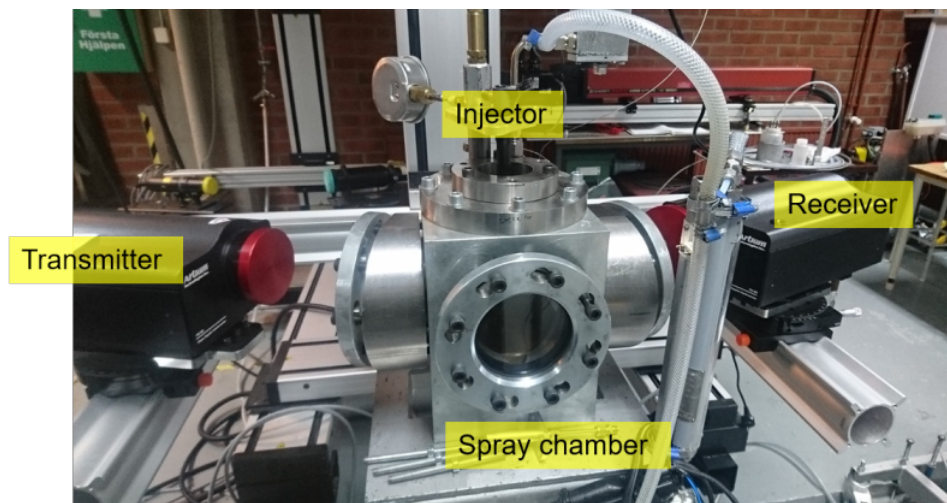


Figure 3.9: The PDI measurement apparatus.

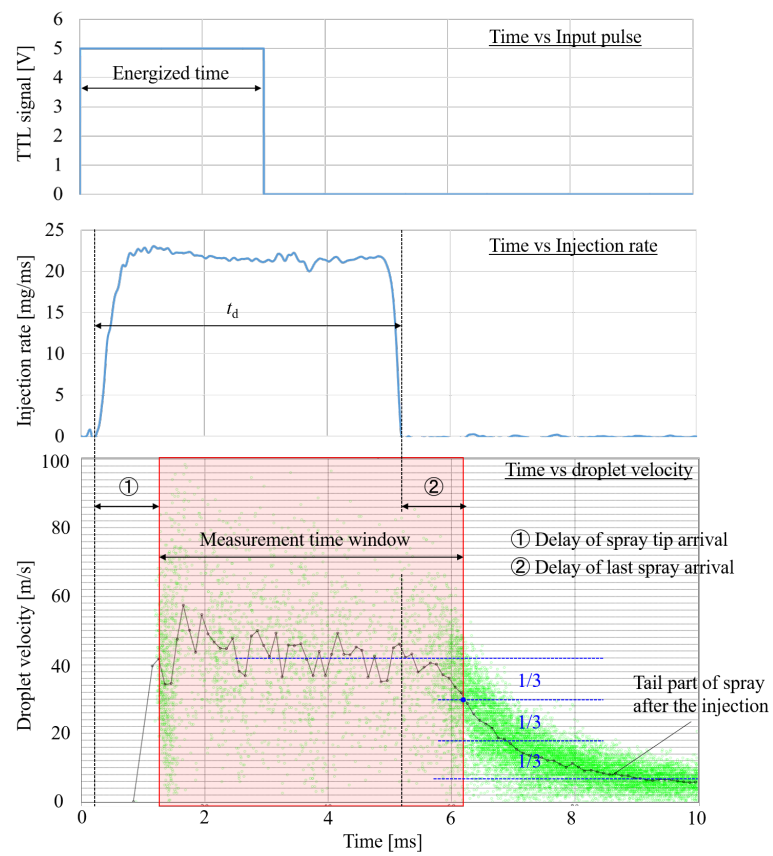


Figure 3.10: Measurement time window for PDI experiments.

Table 3.4: Measurement conditions for Phase Doppler Interferometry.

Parameters	Units	Values
Injector		Divergent 6 hole
Fuel type		n-heptane
Fuel temperature	K	293
Fuel pressure	bar	200, 400, 600, 800, 1000, 1200, 1500
Chamber gas		air
Chamber gas temperature	K	293
Chamber gas pressure	bar	1
Energizing time	ms	3
Wavelength of lasers	nm	532, 561
Focal length of transmitter	mm	350
Beam diameter	mm	2.33
Expander factor		1.00
Frequency shift	MHz	40
Collection angle (refractive mode)	degree	34
Static range	$\mu\text{m}$	0.6 - 93.7
Index of refraction		1.45
Measured number of droplets		> 10000
Measuring range	$\mu\text{m}$	0.6 - 93.7
Size accuracy	$\mu\text{m}$	$\pm 0.5$
Size resolution	$\mu\text{m}$	$\pm 0.5$

Three statistical measures (mean values) of droplet size are commonly used in spray analysis: the mean diameter ( $D_{10}$ ), the Sauter mean diameter ( $D_{32}$ ), and the diameter corresponding to a cumulative volume fraction of 90 % ( $Dv_{90}$ ).  $D_{10}$  is the arithmetic mean of the size of all counted droplets; it therefore tends to reflect the size of the most numerous droplets. Consequently, it does not always accurately indicate the abundance of rarer large droplets.  $D_{32}$  is a measure of average droplet size based on droplet volume and surface area. Consequently, the  $D_{32}$  value for a sample containing a single large droplet and many small ones will differ markedly from that for a sample containing only small droplets.  $D_{32}$  is commonly used to compare spray characteristics because it can be considered more representative of the overall droplet size distribution than the mean diameter.  $Dv_{90}$  is the diameter below which 90 % of the observed droplets exist (see Figure 3.11). It can thus be considered a measure of the size of the largest droplets in the spray. Consequently, if  $Dv_{90}$  is 20  $\mu\text{m}$ , the spray will contain almost no droplets with diameters above 20  $\mu\text{m}$ . Measures of droplet size considered in this work include  $D_{10}$ ,  $D_{32}$ , and  $Dv_{90}$  at different injection pressures, the volume fraction distribution, and time-resolved  $D_{32}$  traces.

$$D_{10} = \frac{\sum N_i D_i}{\sum N_i} \quad (3.1)$$

$$D_{32} = \frac{\sum N_i D_i^3}{\sum N_i D_i^2} \quad (3.2)$$

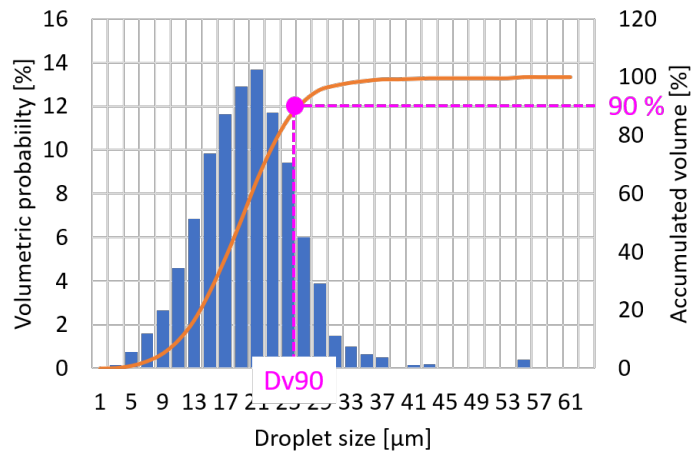


Figure 3.11: A volumetric probability histogram and the definition of  $Dv_{90}$

### 3.6 Particle Image Velocimetry

Particle Image Velocimetry (PIV) was used in this study to investigate spray-induced air motion; the experimental setup used for this purpose is shown in Figure 3.12. PIV is an optical two dimensional flow-field velocity measurement technique and was performed using a system consisting of a double-pulse Nd-YAG laser, CCD camera,

synchronizer, PC, and particle seeder. The laser's second harmonic (532 nm) was used to illuminate regions of the flow field containing seeded particles, and a laser sheet ( $\approx 1$  mm thick) was formed using cylindrical lenses. The relationship between the laser sheet's properties and the capture range is shown in Figure 3.13. The laser sheet passed through the center of a spray plume, and air motion images were captured from the side of the constant volume chamber. The image resolution of the CCD camera was  $2660 \times 1776$  pixels. The synchronizer controlled the activation timing of the laser and camera relative to the injection. The delay between the activation of the 1st and 2nd lasers was set to  $200 \mu\text{s}$  based on the velocity of the target flow and the results of preliminary tests. Spray images were captured at different time points after the start of injection by changing the timing of the injection pulse; 30 images were captured at each timing and averaged. A Laskin-type aerosol generator was used to inject small particles of olive oil into the constant volume chamber through the air intake pipe. It is important when seeding particles to ensure that their size is appropriate for the task at hand because the ability to track seeded particles is central to PIV measurement. The seeder generated small particles, mostly with diameters around  $1 \mu\text{m}$ . Particles of this size are suitable for tracking turbulent or high speed gas flows [40]. The density of the seeded particles in the surrounding air is considerably lower than the density of the liquid droplets in the spray, so the optical signals from the seeded particles in the surrounding air were significantly weaker than those from the spray. Therefore, a physical mask was placed between the constant volume chamber and the camera to block intense scattered light from the spray. Despite this, there was still a strong signal from the spray droplets that made it impossible to detect signals from seeded particles in the area close to the spray. Therefore, the investigations focused on the air flow vectors in a region some distance from the spray edge. Interrogation areas were defined to determine the displacement of the particles in the captured images, using grids small enough that one could reasonably assume the flow to be uniform within them. Recursive analysis was used to increase the accuracy of the measured velocities. Velocity calculations were first performed for a relatively large interrogation area ( $128 \times 128$  pixels) and then for a smaller one ( $64 \times 64$  pixels). The experimental conditions for PIV measurement are listed in Table 3.5.

The output of this method is essentially a vector field in an interrogation area that can be analyzed to calculate air entrainment and the entrained air mass. Air entrainment is the air flow entrained into the spray, which helps drive atomization and mixture formation. In this work, a control line was defined along which air entrainment was calculated. Figure 3.14 shows this control line, which is 40 mm long and positioned 20 mm from the injector axis. This location was selected after a parameter study on the effects of varying the line location and length; the chosen length and location were found to be optimal for capturing trends and differences in air motion at different injection pressures and injection masses. The vectors closest to the control line were selected and their components orthogonal to the line were calculated using Equation 3.3. Air entrainment was computed by averaging the orthogonal components at different time steps (Equation 3.4), and the air entrainment

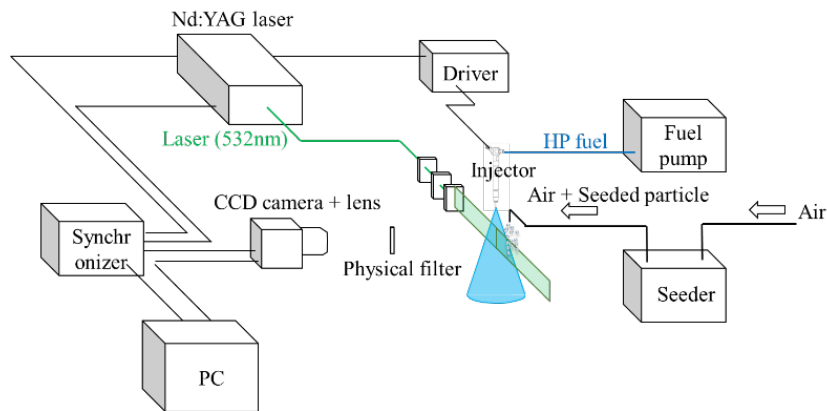


Figure 3.12: Schematic depiction of the PIV setup.

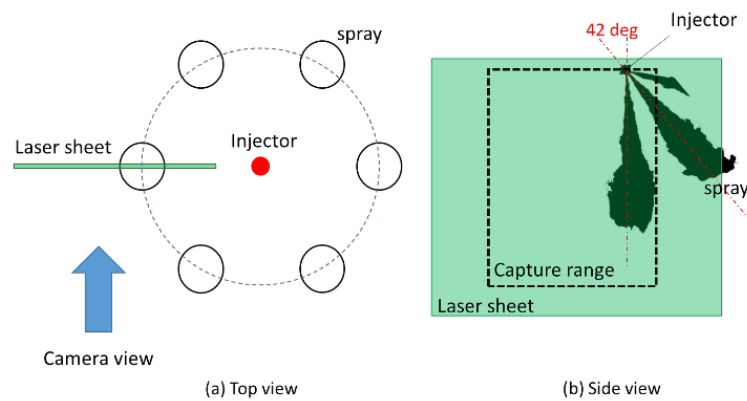


Figure 3.13: Schematic depiction of the spray imaging setup: (a) top view, (b) side view.

Table 3.5: Measurement conditions for PIV measurement.

Parameters	Units	Values
Injector		Divergent 6 hole Convergent 6 hole
Fuel type		n-heptane
Fuel temperature	K	293
Fuel pressure	bar	200, 600, 1000, 1500
Chamber gas		air
Chamber gas temperature	K	293
Chamber gas pressure	bar	1
Seeded particle		Olive oil
Seeded particle size	$\mu\text{m}$	1
Camera resolution	pixel <sup>2</sup>	$2352 \times 1768$
Image resolution	mm/pixel	0.0435
Time delay of two lasers	$\mu\text{s}$	200

at each time step was integrated to obtain the total mass of entrained air moving through the control line (Equation 3.5)

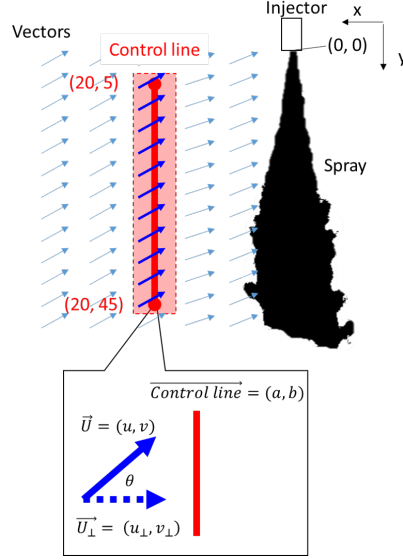


Figure 3.14: Line for air entrainment calculation

$$u_{\perp} = \pm \frac{b(av - bu)}{a^2 + b^2}, v_{\perp} = \pm \frac{a(av - bu)}{a^2 + b^2} \quad (3.3)$$

Here, the air flow vector is  $\vec{U} = (u, v)$ , the component of the air flow vector orthogonal to the control line is  $\vec{U}_{\perp} = (u_{\perp}, v_{\perp})$ , and the control line vector is  $\vec{l} = (a, b)$

$$Q_{\text{entrainment}} = \overline{\sum \rho |\vec{U}_{\perp}|} \quad (3.4)$$

$$m_{\text{entrained}} = \int \sum \rho |\vec{U}_{\perp}| dt \quad (3.5)$$

After calculating the air entrainment rate and the entrained mass, the ratio of the entrained mass to the injection mass was calculated. This ratio is a measure of the amount of air entrained per unit mass injected, and is calculated using equation (3.6).

$$\eta_{\text{entrainment}} = \frac{m_{\text{entrained, max}}}{m_{\text{inj}}} \quad (3.6)$$

### 3.7 Single cylinder optical engine

Spray behavior inside the cylinder was observed using a single cylinder optical engine. A schematic depiction of the apparatus and the test conditions are presented in Figure 3.15 and Table 3.6. The optical engine has optical access from the side and bottom through the glass cylinder and the piston top, respectively. The mass of fuel injected was varied to imitate specific IMEP conditions. For example, an injection

mass of 27 mg is roughly what would be expected for an IMEP of 8-9 bar. The injected sprays were captured with a high-speed video camera, and the obtained images were qualitatively analyzed to determine the positional relationship between the sprays and the walls. Spray images were taken from the side through the glass cylinder wall, and solid state plasma light illuminated the spray from below through the glass piston top. All measurements were conducted without firing.

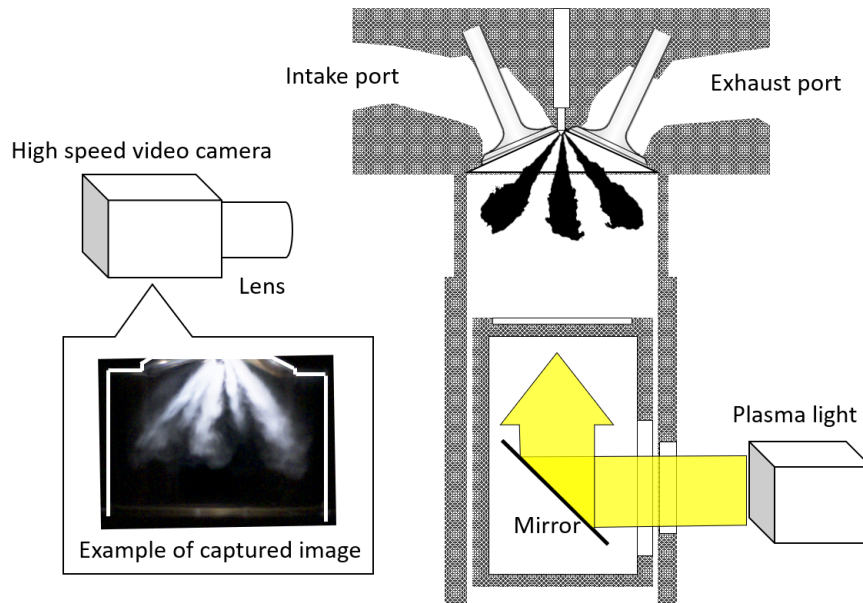


Figure 3.15: Schematic depiction of the optical engine.

### 3.8 Single cylinder metal engine

All thermal experiments were performed using a naturally aspirated single cylinder direct injected metal engine with a four-valve cylinder head (see Figure 3.16). The engine's specifications are given in Table 3.7. Fuel was injected using the diesel injector with a modified nozzle mounted centrally in the cylinder head. The injection pressure was varied between 400 and 1500 bar. A stoichiometric fuel-air mixture and a maximum break torque (MBT) combustion phasing ( $MFB_{50} = 8^\circ \text{aTDC}$ ) were used in all experiments. SCE experiments were conducted under hot, warming-up, and simplified load transient conditions.

PN emissions were measured using a Cambustion DMS500 MkII Differential Mobility Spectrometer, which enables measurements of particles with diameters up to 1000 nm. Legislated PN emissions are usually measured after passage through a volatile particle remover (VPR), but in these experiments the PN emissions at some SOI timings were too low to be detected when using a VPR. Therefore, the DMS500 was directly connected to the exhaust pipe and its inlet was positioned 200 mm downstream of the exhaust valve. Injection pressures above 1000 bar were generated using a diesel pump driven by a motor. Normal gasoline fuel has insufficient lubricity

Table 3.6: Measurement conditions for optical engine test.

Parameters	Units	Values
Fuel type		iso-octane
Cylinder volume	cc	479
Bore	mm	81.4
Stroke	mm	92
Engine head		Four valve SIGDI
Injector		Divergent 6-hole injector
Injection pressure	bar	200, 600, 1000, 1500
SOI timing	°bTDC	340, 300, 270, 240, 210 180, 150, 120, 90, 60
Engine speed	rpm	1750
Injection mass	mg	27
Intake air temperature	K	298
Camera model		Phantom VEO 710S
Lens		Nikon AI AF NIKKOR 50mm f1.8D
Plasma light source		THORLABS HPLS200
Frame rate	fps	49000
Resolution	pixel×pixel	512×256

for use with a diesel pump, so a lubricity improver was added to avoid pump damage. The fuel line system included a common rail installed next to the injector to minimize the pressure drop and pulsation caused by injection. This effect was verified in preliminary experiments using an injection rate meter. The injection pressure was monitored using a pressure sensor located in the pipe between the common rail and the injector to ensure that there was no significant pressure drop inside the pipe during the engine tests. The SCE allows optical access to the cylinder's interior via the endoscope windows. The positions of the endoscope windows and an image captured through these windows are shown in Figures 3.17 and 3.18, respectively. A solid state plasma light was used to illuminate the interior of the cylinder via the exhaust-side endoscope windows and a high-speed video camera was used to capture images via the intake-side endoscope windows. Running the SCE under conditions that generate high particulate emissions (for example, warm-up conditions) led to the formation of grime on the endoscope windows. Therefore, these windows were regularly cleaned during the experiments. The endoscope windows were made from highly heat- and pressure-resistant quartz glass.

### 3.8.1 Procedure for tests under hot and steady conditions

In all engine tests, the engine was made thermally stable by allowing it to run until a steady state was reached before logging any data. The exhaust was sampled with a primary dilution ratio of 5 and a secondary dilution ratio of 1 through a heated



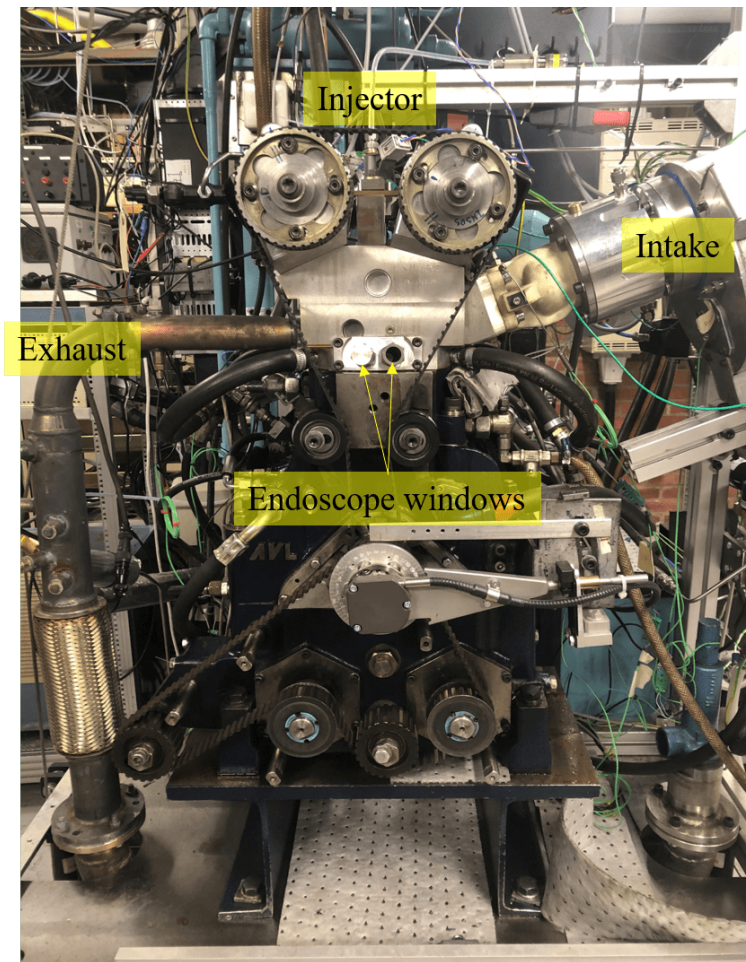


Figure 3.16: Picture of the single cylinder engine.

Windows for endoscope and light

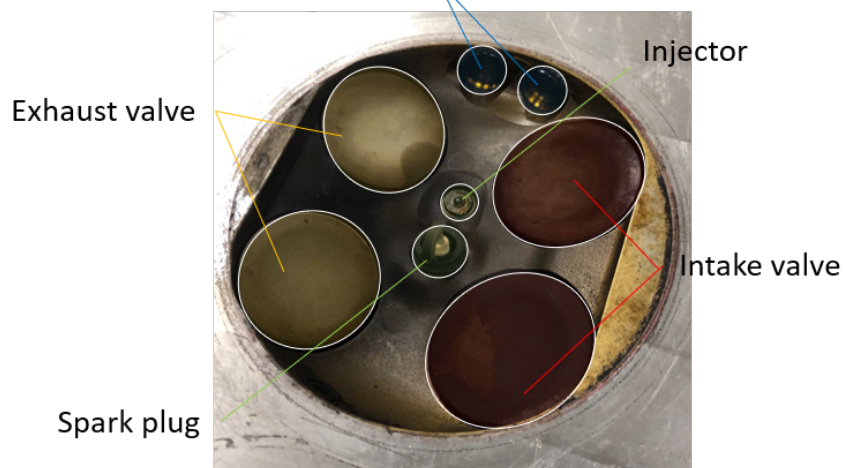


Figure 3.17: Positions of the endoscope windows on the cylinder head

Table 3.7: Properties and settings of the single cylinder metal engine apparatus.

Parameters	Units	Values
Fuel type		Gasoline RON95 E10
Cylinder volume	cc	500
Bore	mm	82
Stroke	mm	90
Engine head		Four valve SIGDI
Operating mode		Stoichiometric combustion
Spark timing		MBT
Intake air temperature	K	298
Inlet valve opening	°aTDC	356
Inlet valve closing	°aTDC	578
Exhaust valve opening	°aTDC	145
Exhaust valve closing	°aTDC	357
Injector		Divergent 6-hole injector Divergent 10-hole injector
Camera		Phantom V1210
Endoscope		LaVision Endoscope
Shutter speed	fps	19000
Capture duration	ms	10
Start of recording		Same timing as spark
Aperture		5.6
Resolution	pixel×pixel	512×464

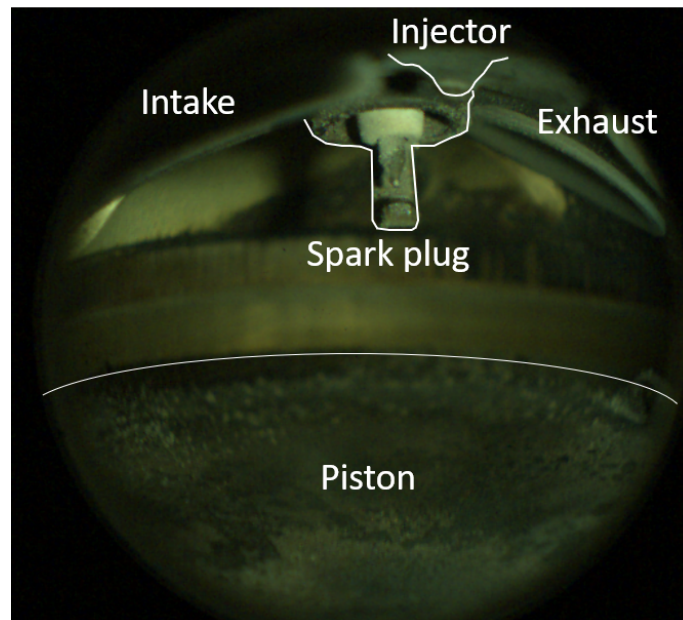


Figure 3.18: Background image of the cylinder interior captured using the HS camera via an endoscope

sampling line maintained at 190 °C. The exhaust gas was sampled 150 mm from the exhaust port. PN counting was performed over a period of at least 3 minutes in all cases to acquire accurate averages.

### **3.8.2 Procedure for warm-up tests**

The engine oil and coolant temperatures were varied between 20 °C and 90 °C. Once the oil and coolant temperatures had stabilized, the engine was made thermally stable by allowing it run until a steady state was reached. The exhaust was then sampled with a primary dilution ratio of 5 and a secondary dilution ratio of 1 through a heated sampling line maintained at 190 °C. The exhaust gas was sampled 150 mm from the exhaust port. PN counting was performed as described for the hot steady state tests. The conditions examined in the warm-up tests are listed in Table 3.8.

### **3.8.3 Procedure for simplified transient tests**

Simplified load transient tests were conducted to evaluate the effects of ultra-high injection pressures on particulate emissions during load transients. During these tests, the SCE was first operated under hot conditions for at least 60 seconds to make the engine thermally stable. The engine was then motored for a designated period (10, 30, or 180 seconds) to establish a specific temperature status. Time-resolved temperature traces for the exhaust and cylinder head after the initiation of motoring are presented in Figure 3.19. The exhaust temperature fell immediately upon initiating motoring, whereas the cylinder head temperature fell more gradually over time. Three different motoring durations were used to establish different exhaust and cylinder head temperatures, as shown in the table presented in Figure 3.19. A timing diagram for these tests is shown in Figure 3.20. Fuel injection and ignition were resumed after the end of the motoring period and the next 100 flames starting from the first firing cycle were recorded using the high-speed video camera. This procedure was repeated 10 times for each motoring duration and the probability of observing a luminous flame in each case was calculated by post-processing of the captured images. The experimental conditions used in the simplified transient tests are specified in Table 3.8.

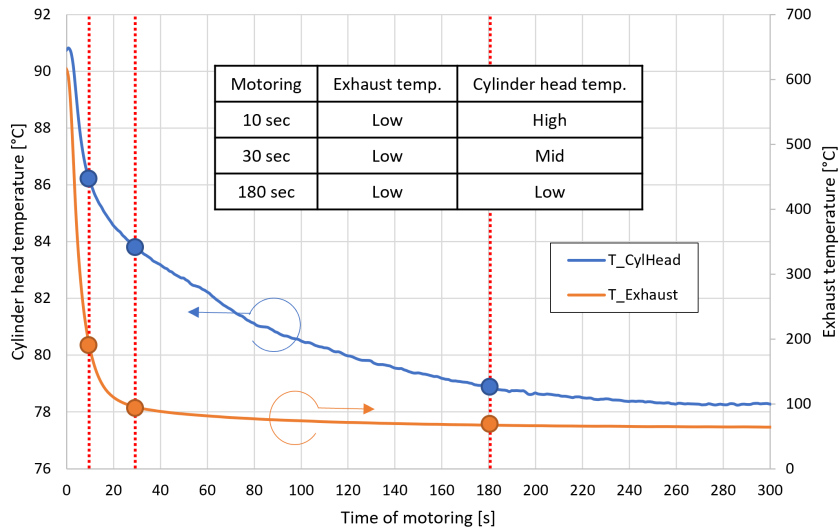


Figure 3.19: Time-resolved exhaust temperature and cylinder head temperature traces after the start of motoring.

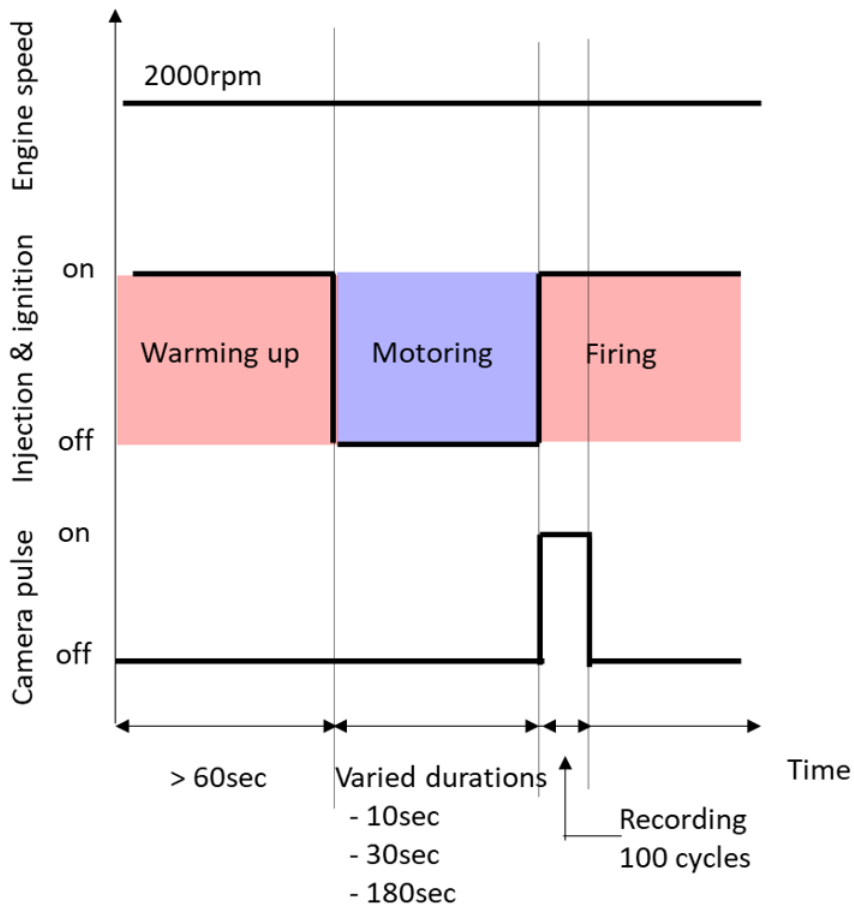


Figure 3.20: Timing diagram of the simplified load transient tests.

Table 3.8: Conditions applied during the simplified load transient tests using the metal engine.

		Hot and Steady	Warm-up	Simplified transient
Fuel pressure	bar	400, 600, 1000, 1500		
Engine speed	rpm	2000	1000	2000
IMEP	bar	9	4.5	9
SOI timing	°bTDC	340, 330, 320, 310, 300 290, 280, 270, 260, 250 240, 230, 220, 210, 200 190, 180, 170, 160, 150 140, 130, 120, 110, 100	300	300
Oil and coolant temperature	°C	80	20, 25, 30, 35, 40 45, 60, 75, 90	80
Duration of motoring	s			10, 30, 180



# Chapter 4

## Summary of publications

This chapter briefly summarizes the contents of the publications arising from the research conducted during this PhD project. The results obtained are discussed holistically and in more detail in the following chapter (Results and Discussion).

### 4.1 Paper I

*"Spray Characterization of Gasoline Direct Injection Sprays Under Fuel Injection Pressures up to 150 MPa with Different Nozzle Geometries"*

Paper I presents experimental studies on the properties of sprays formed at high injection pressures. Spray characteristics such as the spray tip penetrations and droplet size distribution were determined as functions of the fuel injection pressures. The experiments were conducted using optical measurement techniques in a constant volume spray chamber: spray tip penetration was measured by high speed video imaging and two-component PDI was used for droplet size and velocity measurement. The results showed that increasing the fuel pressure increased the spray velocity, leading to higher spray tip penetration. However, the penetration length was more sensitive to the nozzle hole shape and ambient pressure than the injection pressure. Divergent nozzle holes tended to form wider sprays than straight and convergent nozzle holes, causing more momentum exchange with surrounding air. Increased fuel pressures enhanced atomization, which would be expected to improve air-fuel mixing and increase the rate of evaporation of liquid fuel in a real engine.

The author of this thesis constructed the apparatus used in these experiments at Chalmers Tekniska Högskola (CTH) with support from Patrik Wåhlin, performed all experiments and post-processing, wrote the paper, and presented the paper at the SAE Powertrains, Fuels and Lubricants meeting in San Antonio, Texas. The work presented in this publication was supervised by Petter Dahlander, Lucien Koopmans, Fabian Peng-Kärrholm, and Ayolt Helmantel.

## 4.2 Paper II

*"Air Motion Induced by Ultra-High Injection Pressure Sprays for Gasoline Direct Injection Engines"*

Paper II explores the effects of high pressure sprays on the surrounding air by quantifying air entrainment in the near-nozzle region. The PIV technique was used to capture the two-dimensional velocity field of the spray-induced air motion. In Paper I, it was shown that higher fuel pressures result in higher spray velocities. Accordingly, the induced air motion and the mass of air entrained into the spray both increased with the injection pressure; the amount of air entrainment caused by injecting only 5 mg of fuel at 1500 bar was similar to that caused by injecting 27 mg at a pressure of 200 bar. However, the induced air motion fell quickly after the EOI, reaching a similar level for all injection pressures. The air entrainment rate was also increased by using a divergent nozzle rather than a convergent one. The interactions between the spray and the surrounding air are thus strengthened by using a high injection pressure and a divergent nozzle.

In the Paper II, the author of this thesis constructed the experimental setup at CTH with support from Patrik Wåhlin, performed all of the experiments and post-processing, and wrote the paper for SAE International Journal of Fuels and Lubricants. The work presented in this publication was supervised by Petter Dahlander, Lucien Koopmans, Johan Dillner, and Ayolt Helmantel.

## 4.3 Paper III

*Spray behaviors and GDI engine performances using ultra-high injection pressure up to 1500 bar*

Paper III presents a comprehensive study on high pressure sprays including measurements of basic spray characteristics and experiments using an optical engine and a single cylinder engine. The experimental techniques used in the spray measurements in their main outputs were basically identical to those discussed in Papers I and II. The optical engine tests and thermal tests were conducted using single cylinder engines to capture actual spray behavior inside the cylinder and its impact on emissions and engine performance. The optical engine tests showed that high pressure sprays retained their shape in the presence of a strong intake air flow more effectively than sprays formed at lower pressures such as 200 bar. This makes it possible to ensure that sprays plumes follow specific desired trajectories even when there is a strong tumble flow. Independently of the injection pressure, there was no clear contact between the sprays and the piston when the SOI timing was later than 300 °bTDC. Thermal tests revealed that the combustion stability, HC emissions, and PN emissions all improved upon increasing the injection pressure over a wide range of SOI timings. These improvements were attributed to better mixture formation and reduced wall film formation, leading to more complete combustion.

The author of this thesis constructed the experimental setup for the spray chamber and the single cylinder metal engine at CTH with the support of Patrik Wåhlin and Alf Magnusson, and performed the experiments and post-processing. The author also



set up the optical engine and performed the optical experiments with support from Martin Eriksson at Volvo Cars. The author wrote the paper for the SAE International Journal of Engines. The work presented in this publication was supervised by Petter Dahlander, Lucien Koopmans, Johan Dillner, and Ayolt Helmantel.

## 4.4 Paper IV

*High fuel injection pressure effect on warming-up and simplified load transient conditions in gasoline direct injection engines*

Paper IV extends the engine tests presented in Paper III, focusing on two important engine operating conditions: warming-up and simplified load transients. Together with cold starts, these operating conditions are responsible for the majority of the total particulate emissions over a driving cycle. Paper IV therefore investigates the effects of ultra-high injection pressures on emissions and engine performance under these conditions. To mimic warming-up conditions, SCE tests were performed with low coolant temperatures under low load conditions. The results of these tests showed that increasing the fuel pressure reduced emissions, but the emissions were more sensitive to the coolant temperature than to the fuel pressure. The simplified load transient tests revealed that the occurrence of luminous flames depends on the injection pressure and the motoring duration. Luminous flames were observed more frequently from the intake valves and piston top when the cylinder temperature was low due to prolonged motoring. Low wall temperatures hindered wall film vaporization, and the residual liquid films on the walls gave rise to luminous flames. These luminous flames generally faded away within a few seconds, but the rate at which they disappeared increased with the fuel pressure.

The author of this thesis constructed the experimental setup at CTH with the support of Alf Magnusson, performed the experiments and post-processing, and wrote the paper. The work presented in this publication was supervised by Petter Dahlander, Lucien Koopmans, Johan Dillner, and Ayolt Helmantel.



# Chapter 5

## Results and Discussion

This thesis is based on experimental investigations into the effects of ultra-high fuel injection pressures on spray behavior, emissions, and engine performance in GDI engines. The experiments mainly consisted of spray and engine tests. Spray tests were performed in a constant-volume chamber to determine how ultra-high fuel pressures affect spray characteristics, while engine experiments were performed to determine the effects of high fuel pressures on emissions and engine performance. This chapter summarizes the results obtained during these studies.

### 5.1 Spray test

The first half of the PhD project focused investigating spray characteristics using a constant-volume chamber. In preparation for the spray tests, injection flow rates were measured to determine the relationship between injection duration and injection mass.

#### 5.1.1 Spray tip penetration

Spray tip penetration is the distance between the injector nozzle tip and the spray tip, and is a key variable for describing spray behavior. Moreover, penetration measurements are widely used to validate CFD spray models. In the constant volume chamber experiments, penetration lengths were measured by post-processing of shadowgraph images. The injection mass was kept constant during these experiments, so the injection duration varied with the injection pressure. Figure 5.1 shows spray images acquired at EOI timing with four different nozzle shapes at ambient pressures of 1 and 6 bar. For all nozzle shapes, increasing the injection pressure caused the sprays to become wider and denser. Additionally, sprays from divergent nozzles tended to be shorter and wider than those from convergent and straight nozzles. Raising the ambient pressure from 1 to 6 bar significantly affected the spray shape but did not affect the differences in spray shape between the different nozzle types. Sprays emitted from nozzles with large outlets, i.e. divergent nozzles, were wider from those originating from nozzles with narrow outlets. The relationship between

nozzle shape and spray shape can be attributed to differences in the internal nozzle flow.

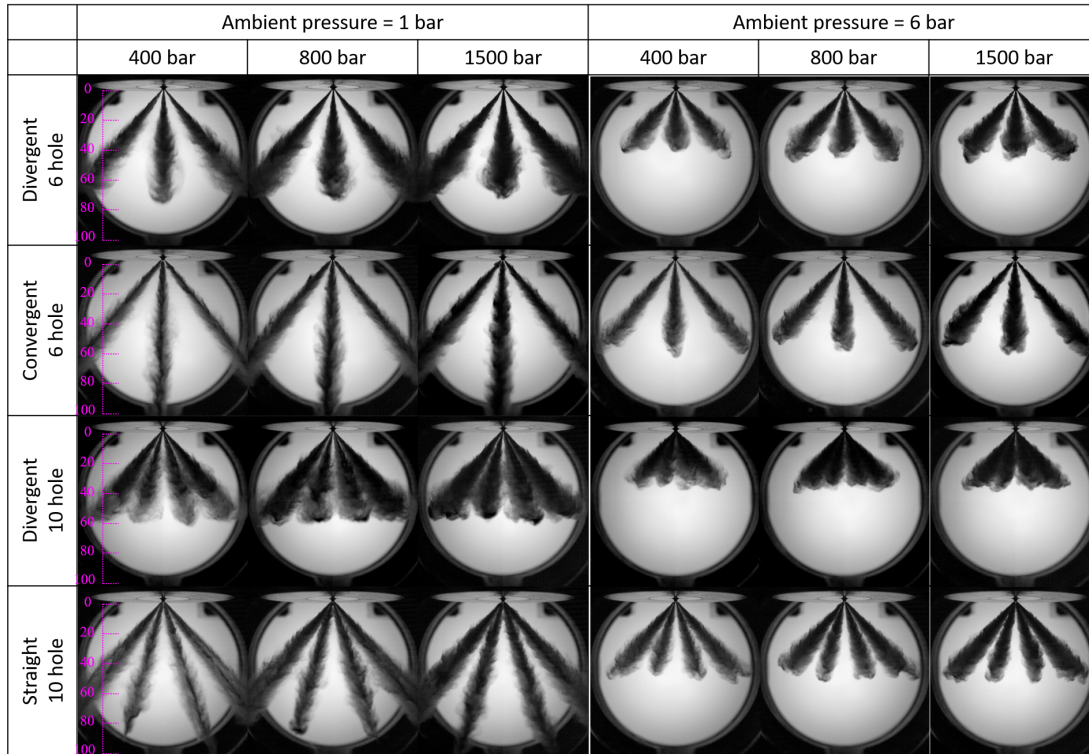


Figure 5.1: Spray images obtained using four different nozzle geometries at EOI timing.

Time-resolved spray tip penetration measurements were obtained by post-processing of spray images. To illustrate how nozzle shape affected spray penetration, the measured penetration lengths for divergent and convergent 6-hole nozzles at ambient pressures of 1 and 6 bar and various injection pressures are shown in Figures 5.2 and 5.3. Generally, sprays formed at higher injection pressures developed much more rapidly than those formed at lower injection pressures. Additionally, there is a clear difference in spray tip penetration between the two nozzle types: the sprays from the divergent nozzle tend to have lower penetration than those from the convergent nozzle due to the different spray shapes generated by each nozzle type (see Figure 5.1). Wider sprays interact more strongly with the surrounding air, leading to shorter penetration lengths. Raising the ambient pressure to 6 bar also strengthens the interactions between the sprays and the surrounding air, leading to significant shortening of the penetration length.

### 5.1.2 Droplet size

A fuel spray's droplet size has important effects on evaporation and mixture formation. The effects of ultra-high injection pressures on droplet size were therefore investigated, yielding the results shown in Figure 5.4. Briefly, increasing the injection pressure had a clear beneficial effect on droplet size. The mean diameter

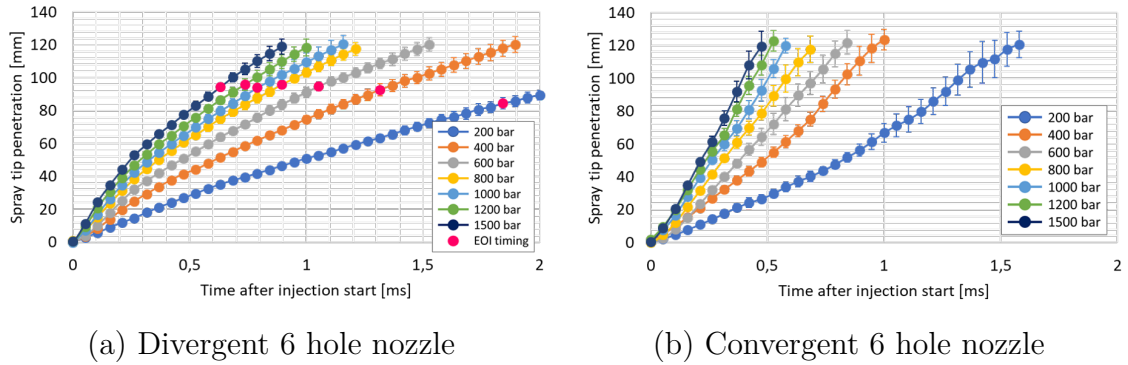


Figure 5.2: Spray tip penetration for different nozzle shapes at an ambient pressure of 1 bar.

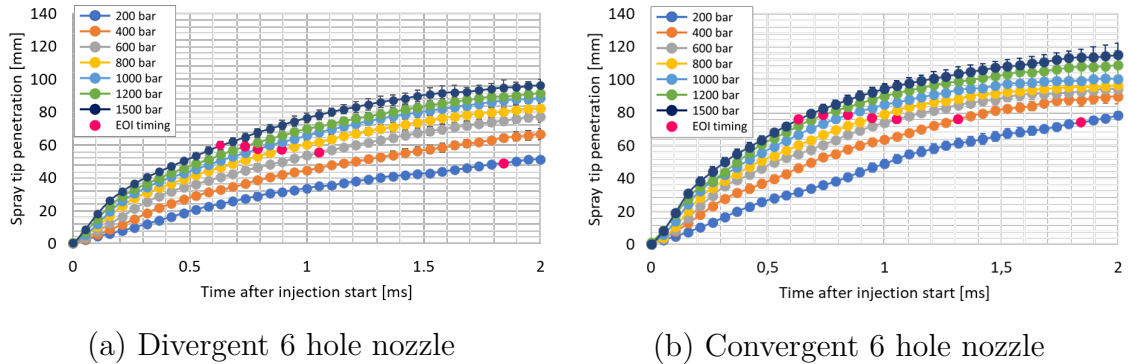


Figure 5.3: Spray tip penetration for different nozzle shapes at an ambient pressure of 6 bar.

( $D_{10}$ ) changed less significantly than the  $D_{32}$  and  $Dv_{90}$ , both of which decreased significantly as the injection pressure was raised. The reduction in these parameters was especially pronounced upon raising the injection pressure from 200 bar to 600 bar; less substantial increases were observed upon raising the injection pressure above 1000 bar. This suggests that the majority of the droplets are small under all pressure conditions, but the low pressure sprays contain some large droplets that increase  $D_{32}$  and  $Dv_{90}$ . The dependence of the droplet size on the injection pressure is shown in Figure 5.5, where the droplet size distribution at an injection pressure of 400 bar is taken as a baseline case. Upon raising the injection pressure from 400 bar to 1500 bar,  $D_{10}$  is reduced by 25%,  $D_{32}$  by 30%, and  $Dv_{90}$  by 40%. The reduction in droplet size upon raising the injection pressure can mainly be attributed to unstable flow inside the nozzle and the increased velocity of the spray relative to that of the surrounding air. The velocity inside the nozzle increases with the injection pressure, increasing the strength of the cavitation forces at the nozzle inlet. This cavitation creates a turbulent flow at the nozzle outlet, which can help break up large droplets and ligaments into smaller droplets in the near-nozzle region. As a result, atomization in the downstream region of the spray is improved. The high velocity of the spray relative to the surrounding air also facilitates break-up because individual droplets break up when the aerodynamic force resulting from their

interaction with the surrounding air becomes stronger than the consolidation force. The aerodynamic force depends on the density of the air and the relative velocity of the droplet. Therefore, high velocity droplets break up rapidly. However, spray atomization is more complex than this simple picture suggests because collisions and recoupling occur in parallel to breakup. Consequently, there is rarely a simple linear relationship between break-up and injection pressure.

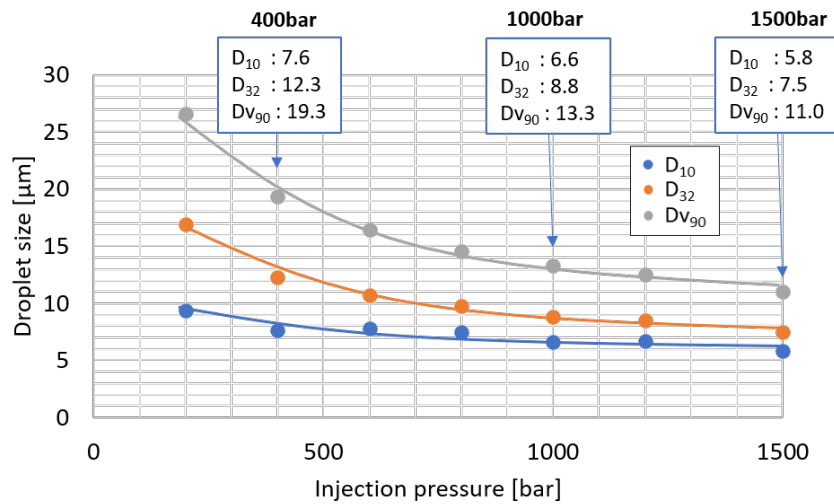


Figure 5.4: Dependence of droplet size on the injection pressure.

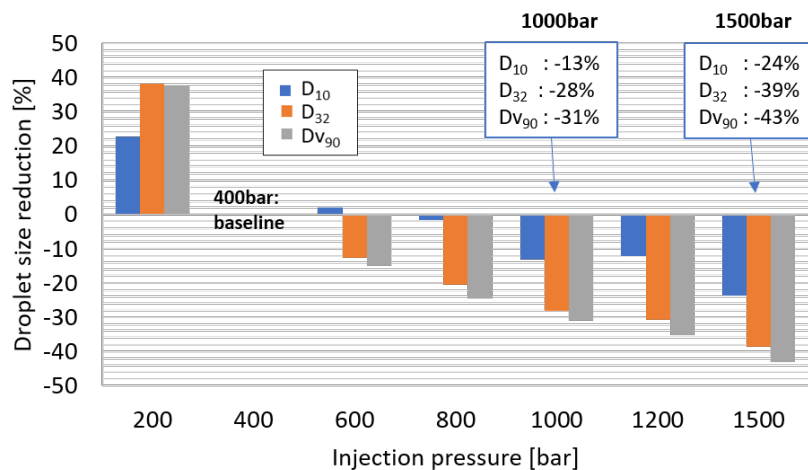


Figure 5.5: Changes in droplet size with injection pressure relative to the baseline size distribution observed at an injection pressure of 400 bar.

### 5.1.3 Spray-induced air motion

The effect of high pressure sprays on the air motion was investigated in Paper II. Spray-induced air motion was studied using two-dimensional PIV, and air entrainment was quantified by analyzing the vector field of the air flow. Figure 5.6 shows the

vector fields of the air motion observed at different injection pressures when using the divergent 6 hole nozzle. It is readily apparent that the velocity and motion of the surrounding air increased with the injection pressure. Particularly high air velocities are seen around the flow entrained into the spray in the near-nozzle region. This entrainment was driven by the recirculating spray-induced air flow and the negative pressure generated by the movement of the spray plume. The spray-induced air flows weakened after the EOI and reached similar levels for all injection pressures by 1.5 ms after SOI. Quantified air entrainment rates calculated on the basis of the magnitudes of the vectors projecting towards the spray are shown in Figure 5.7. Strictly speaking, it may not be correct to talk about "air entrainment" after the EOI because the spray ceases to exist when the injection is terminated. However, for simplicity we will use the phrase "air entrainment" to refer to the movement of air into the fuel-rich region of the cylinder both before and after EOI. The air entrainment rate increased immediately after the SOI and kept increasing throughout the injection event, reaching a maximum around the EOI timing and then falling rapidly after EOI. The maximum air entrainment rate at an injection pressure of 200 bar was significantly lower than that when the injection pressure was 1000 bar. However, raising the injection pressure from 1000 bar to 1500 bar had almost no effect on entrainment. This indicates that air entrainment depends on the duration of the injection as well as the injection pressure; a source of momentum is needed to sustain entrainment and to prevent the entrainment flow from reaching an equilibrium state. It should be noted that the spray was injected into a quiescent air field in this work. However, the air inside the cylinders of a working engine would not be quiescent at all. Therefore, this study should be seen as a fundamental investigation of the interaction between a spray and the surrounding air.

## 5.2 Optical engine results

Spray behavior inside the cylinder was investigated using an optical engine. Spray images were captured with a high-speed video camera, and the positional relationship between the spray and the piston/liner was evaluated qualitatively. Figure 5.8 shows spray images at EOI timing for different SOI timings and injection pressures. At an SOI timing of 340 °bTDC, significant spray impingement on the piston was observed when the injection pressure exceeded 600 bar. Even at the lowest tested injection pressure of 200 bar, the spray touched the piston top at this very advanced SOI timing, in part because the injection was delayed: the injector used in these experiments was a diesel-type model in which the injection is driven by the difference between the injection pressure and the ambient pressure. Consequently, the injection delay decreased as the injection pressure increased. At other SOI timings, the distance between the nozzle and the piston during injection was sufficient to prevent detectable impingement of the spray on the piston irrespective of the injection pressure.

The shapes of the sprays formed at 200 bar clearly differed from those formed at higher injection pressures. An injector with a multi-hole nozzle was used in these experiments, so each injection should in principle generate multiple distinct spray plumes that develop in different directions. However, the trajectories of the low

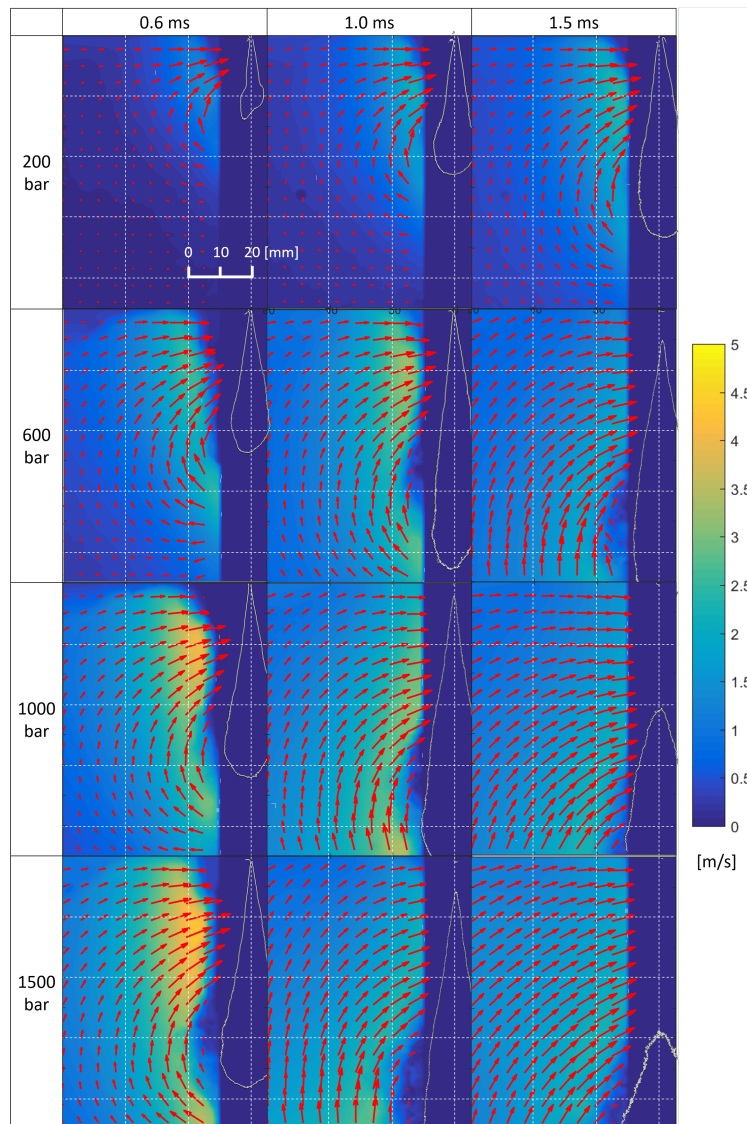


Figure 5.6: Vector fields of the air around the spray at different injection pressures with a 27 mg injection mass

pressure spray plumes were affected by the intake air flow, leading to the formation of aggregated cloud-like sprays without distinct plumes. Sprays formed at injection pressure above 600 bar retained their original shapes because their momentum was greater than that of the intake air flow, so each plume was able to develop fully before being deformed by the air flow. It should be noted that the intensity of the intake air flow depends on the crank angle, so its influence can be reduced by choosing an SOI timing less advanced than  $240^\circ$  bTDC.

These results suggest that increasing the injection pressure improves the spray's ability to withstand the deforming effect of the intake air flow. However, because high injection pressures result in highly penetrating sprays, there is a risk of increased wall film formation on the cylinder liner and piston. The SOI timing and spray targets must therefore be chosen carefully to minimize wall film formation. As a



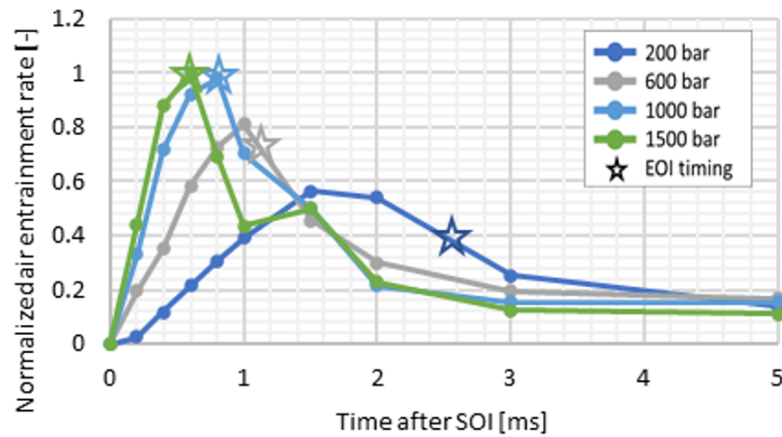


Figure 5.7: Normalized air entrainment rates at different injection pressures with a 27 mg injection mass

result, the SOI should be later than  $300^{\circ}\text{bTDC}$ , at least in the tested engine.

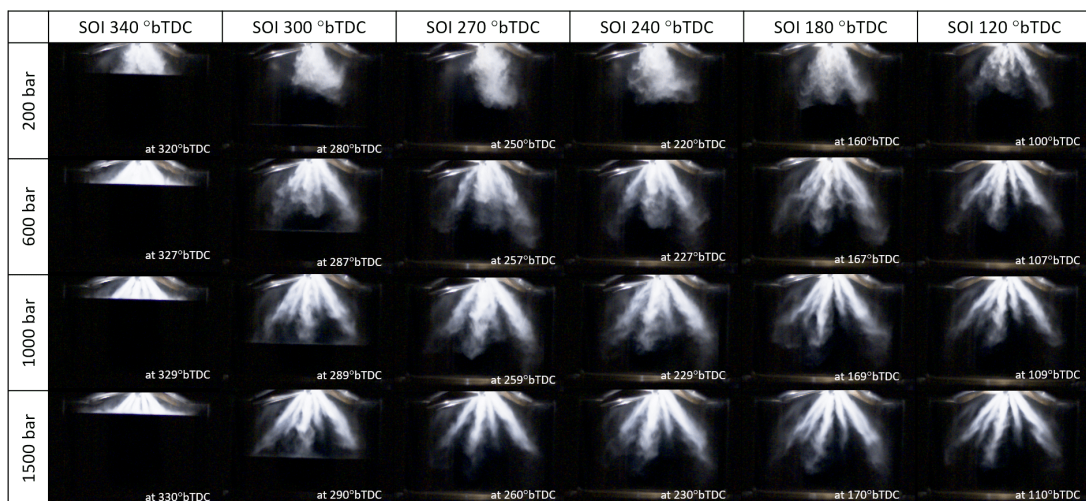


Figure 5.8: Spray images at EOI for sprays formed at different injection pressures and SOI timings

### 5.3 Metal engine results

The effect of high injection pressures on combustion and gaseous/particulate emissions was investigated using a single cylinder metal engine. The highest particulate emissions during a driving cycle occur under cold-start, warm-up, and load transient conditions. In this work, hot conditions were initially examined to determine the basic effect of high pressures on engine performance and emissions. Engine tests were then performed under warm-up and simplified load transient conditions to determine

whether the use of ultra-high injection pressures remains beneficial in these more challenging cases.

### 5.3.1 Hot conditions

Figures 5.9, 5.10, and 5.11 show the dependence of the coefficient of variation in IMEP, HC emissions, and PN emissions, respectively, on the injection pressure and the SOI timing. At commonly used SOI timings around 300 °bTDC, the effect of varying the injection pressure is relatively modest. However, more pronounced differences are seen if the SOI timing is advanced to 340 °bTDC or retarded to 180 °bTDC or later.

The difference seen at retarded SOI timings can be attributed to mixing speed and quality: high injection pressures accelerate the mixing process by increasing air entrainment and the rate of atomization. This increases flexibility in the choice of SOI timings, which may be beneficial when using a multiple injection strategy. The optical engine tests showed that there was appreciable impingement of the spray on the piston when using an advanced SOI timing of 340 °bTDC. The resulting fuel film formation would be expected to increase HC and PN emissions, and such increases were indeed observed when the injection pressure was below 1000 bar. However, the increase was not seen when the injection pressure was above 1000 bar. This may be because high injection pressures somehow cause the fuel film on the piston to evaporate rapidly before ignition. Previous studies have shown that increasing the injection pressure causes the wall films formed upon spray impingement to be wider and thinner than they would be otherwise, and that such wide and thin films evaporate more rapidly than thick and narrow films [27, 53, 55]. Therefore, the fuel films formed by the high pressure sprays at advanced SOI timings may evaporate before TDC, explaining why there was no detectable increase in HC and PN emissions. These results show that the use of high injection pressures enhances the robustness of combustion and enables low-emission operation over a wider range of SOI timings than would otherwise be possible. Thus, in addition to reducing emissions, high injection pressures can increase flexibility in terms of choosing injection timings and strategies.

Figure 5.12 shows how the fuel consumption varies with the injection pressure and SOI timing. While this figure suggests that raising the injection pressure to 1000 bar reduced fuel consumption, it should be noted that the plotted values do not account for the fuel pump work because the ultra-high fuel pressures used in the experiments were generated by the research pump. The pump work needed to generate a given injection pressure can be estimated using the approach described by Husted [22] (see Figure 5.13), who calculated the pump power needed to generate injection pressures up to 400 bar. In this work, Husted's approach was used to estimate the pump power needed to generate injection pressures up to 1500 bar. To account for the effect of the fuel pump work, the pump power was subtracted from the measured engine output power and the fuel consumption was recalculated using the updated power outputs, giving the results plotted in Figure 5.14. After this correction, the improvement in fuel consumption upon raising the injection pressure

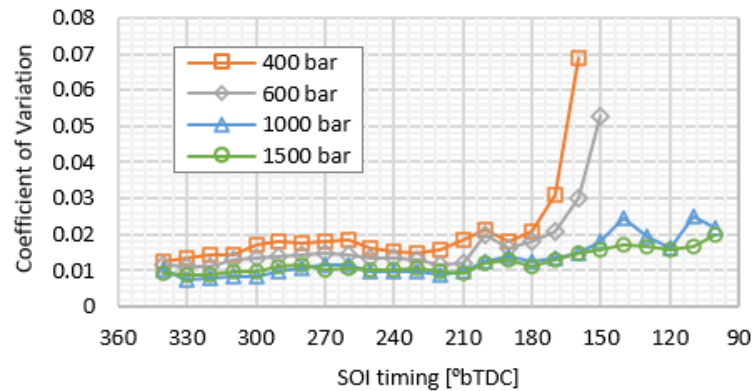


Figure 5.9: CoV in IMEP for various SOI timings and injection pressures at 2000 rpm and 9 bar IMEP under stoichiometric combustion conditions

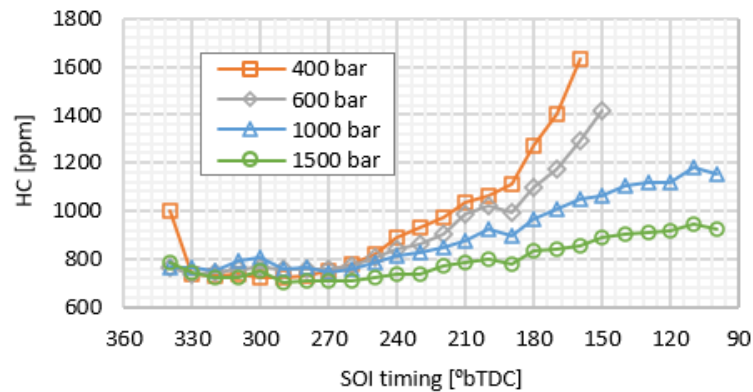


Figure 5.10: HC emissions for various SOI timings and injection pressures at 2000 rpm and 9 bar IMEP under stoichiometric combustion conditions

to 1000 bar was lessened, particularly for SOI timings between 340 and 220 °bTDC. However, a clear benefit remained at more retarded SOI timings.

### 5.3.2 Warm-up condition

The warming-up phase is a major contributor to overall PN emissions over a driving cycle. This phase is characterized by relatively low cooling water and engine oil temperatures. Therefore, the effects of high injection pressures on emissions and engine performance were investigated while controlling the coolant and engine oil temperature to mimic warming-up conditions. Combustion characteristics and gaseous/particulate emissions were measured in same manner as in the engine tests under hot and steady conditions. The HC emissions observed in these experiments are shown as a function of the coolant temperature in Figure 5.15. This figure shows that HC emissions increase at lower coolant temperatures due to poor vaporization of the liquid fuel, and that the reduction in HC emissions caused by increasing the

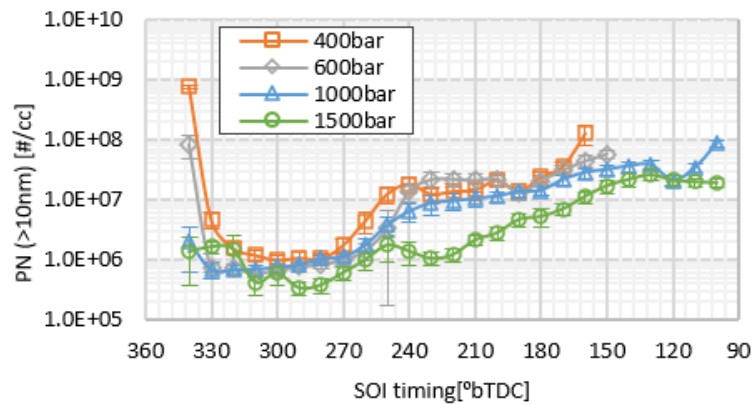


Figure 5.11: PN emissions for various SOI timings and injection pressures at 2000 rpm and 9 bar IMEP under stoichiometric combustion conditions

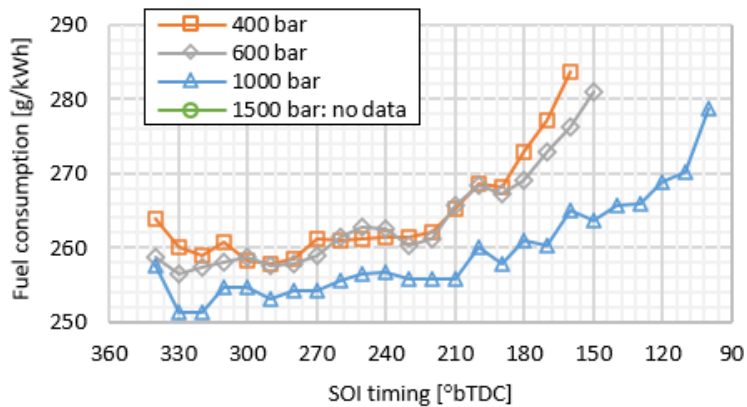


Figure 5.12: Fuel consumption for various SOI timings and injection pressures at 2000rpm and 9 bar IMEP under stoichiometric combustion conditions without considering fuel pump work

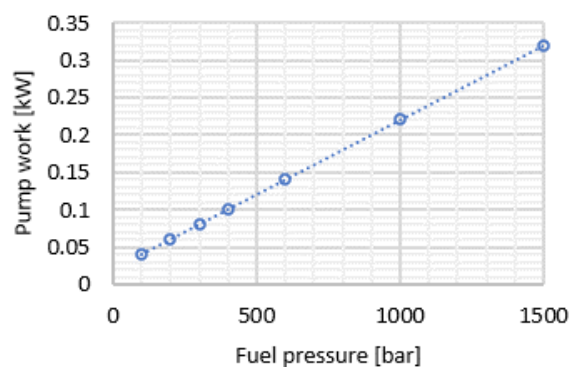


Figure 5.13: Estimated pump work during steady state engine operation based on Husted's work [22]

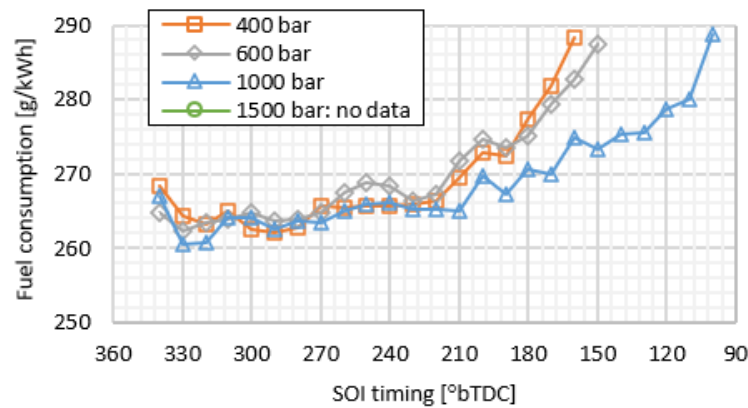


Figure 5.14: Indicated specific fuel consumption for various SOI timings and injection pressures at 2000rpm and 9 bar IMEP under stoichiometric combustion conditions after accounting for pump work

injection pressure is much less pronounced than that caused by increasing the coolant temperature. HC emissions under cold conditions originate mainly from the liner, piston, and fireland [32], and previous investigations have shown that the improved mixing and reduced wall film formation caused by raising the injection pressure are outweighed by the negative effects of low wall temperatures under cold start conditions, leading to an overall increase in emissions [61]. It should also be noted that high coolant temperatures increase the maximum combustion temperature, leading to high NO<sub>x</sub> emissions as shown in Figure 5.16. In summary, the high fuel pressures tested in this work provided no significant benefits in terms of HC and NO<sub>x</sub> emissions.

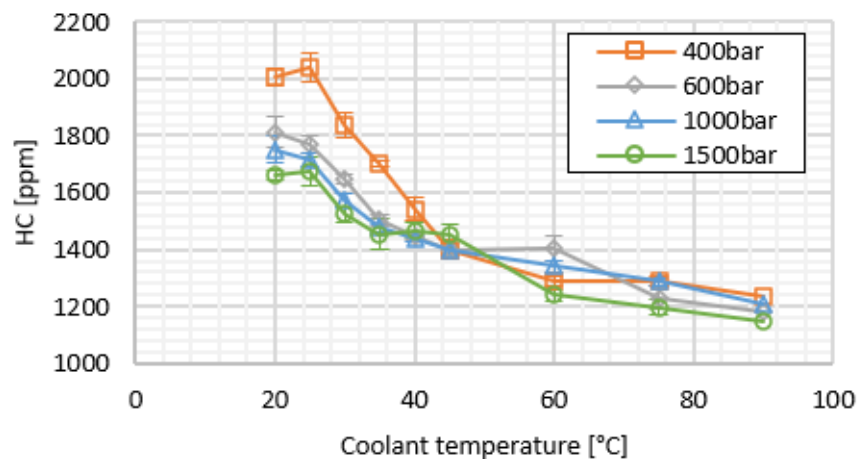


Figure 5.15: HC emissions for various coolant temperatures and injection pressures at 1000 rpm and 4.5 bar IMEP under stoichiometric combustion conditions

Particle number emissions (>23 nm) at various injection pressures are plotted

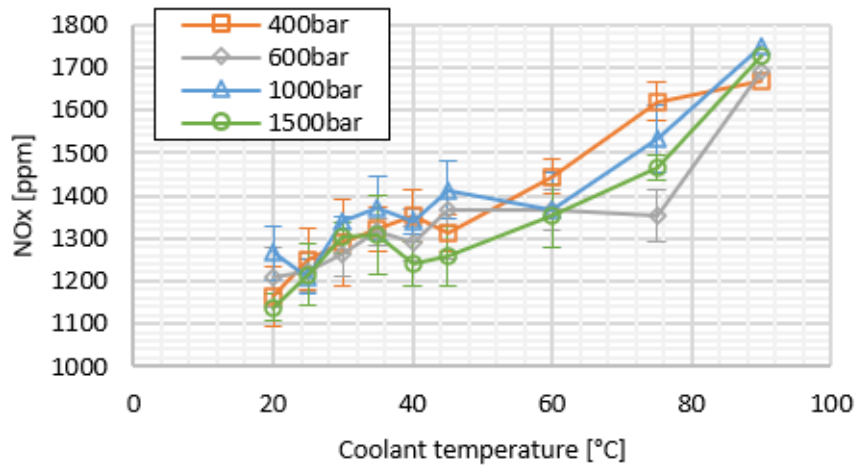


Figure 5.16: NO<sub>x</sub> emissions for various coolant temperatures and injection pressures at 1000 rpm and 4.5 bar IMEP under stoichiometric combustion conditions

as functions of the coolant temperature in Figure 5.17. Counts of emitted particles smaller than 23 nm may include both solid particles and particles consisting of aggregated volatile substances such as unburned HC, which cannot be fully removed without the use of a volatile particle remover. Therefore, to avoid confusion, only results for particles with diameters above 23 nm are plotted. The results presented in Figure 5.17 indicate that lower coolant water temperatures led to higher PN emissions. PN emissions were reduced significantly when the coolant temperature exceeded 60 °C at an injection pressure of 400 bar, or when the coolant temperature reached 45 °C for fuel pressures of 600 and 1000 bar. Interestingly, low PN emissions were observed at all coolant temperatures when the injection pressure was 1500 bar. The injection pressure dependence of the PN emissions could be due to differences in atomization and wall film thickness: higher fuel pressures lead to more efficient atomization and thus reduce wall film formation. Previous studies have also shown that low pressure injection generates large droplets and relatively narrow sprays, resulting in small but relatively thick wall films. Conversely, high pressure sprays are well atomized and wide, resulting in wide and thin wall films [53, 55] that evaporate more rapidly than thick films [27, 61]. This may explain the higher HC and PN emissions at lower temperatures. However, it is not clear why PN emissions were so low even at a coolant temperature of 20 °C when the injection pressure was 1500 bar. Further studies on spray behavior and mixture formation at low temperatures are needed to explain this observation.

### 5.3.3 Simplified load transient conditions

The relative frequencies at which luminous flames were detected for various motoring durations and injection pressures during the simplified load transient experiments were calculated by post-processing of images, giving the results presented in Figure 5.18. For each combination of motoring duration and injection pressure, images were

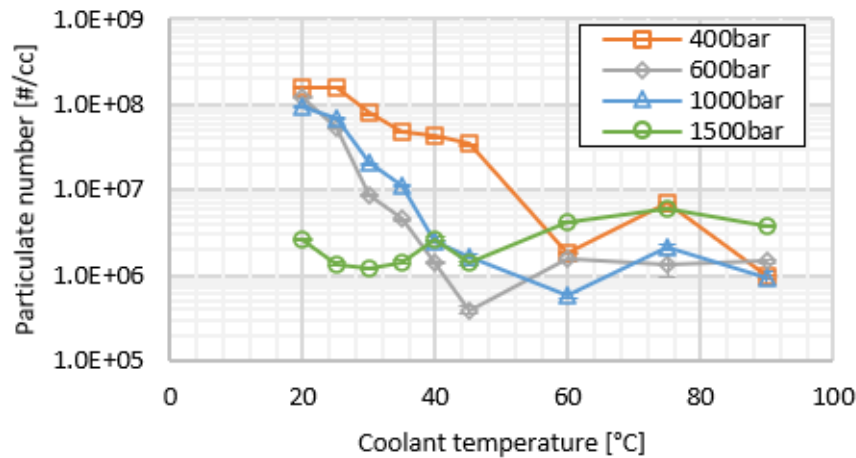


Figure 5.17: Particle number ( $> 23$  nm) emissions for various coolant temperatures and injection pressures at 1000 rpm and 4.5 bar IMEP under stoichiometric combustion conditions

captured over the first 10 cycles after the end of motoring in 10 replicate experiments. When the motoring time was short (10 seconds), no yellow flames were detected inside the cylinder during the subsequent firing cycles. Yellow flames are formed in fuel-rich areas; their absence indicates that evaporation was efficient when the motoring period was short, leading to minimal wall film deposition. When the motoring period was increased to 30 or 180 seconds, luminous flames were most frequently observed around the intake valve and piston. In addition, the frequency at which luminous flames were seen and their spatial extent both increased with the duration of motoring. The injector used in these experiments had a symmetrical 10-hole nozzle that was not designed for the SCE used in the experimental system. Therefore, the spray directions were not perfectly optimal; this mismatch caused significant impingement of the sprays on the intake valve, explaining the formation of luminous flames. Such valve wetting could in principle be avoided by optimizing the orientation of the nozzle holes. The frequency at which luminous flames originating from wall films were observed near the piston increased significantly with the motoring time; this can be attributed to the reduction in wall temperature over longer motoring periods. Unlike the warm-up experiments, the simplified load transient tests were performed at 2000 rpm and 9 bar IMEP (corresponding to an injection mass of  $\approx 28$ mg/cycle), which reduced the mixing time and increased the spray's impingement on the piston. The frequency at which luminous flames were seen increased as the injection pressure decreased, presumably for reasons similar to those invoked when explaining the results of the warming-up experiments: higher injection pressures lead to better atomization and the formation of thinner fuel films that evaporate more readily.

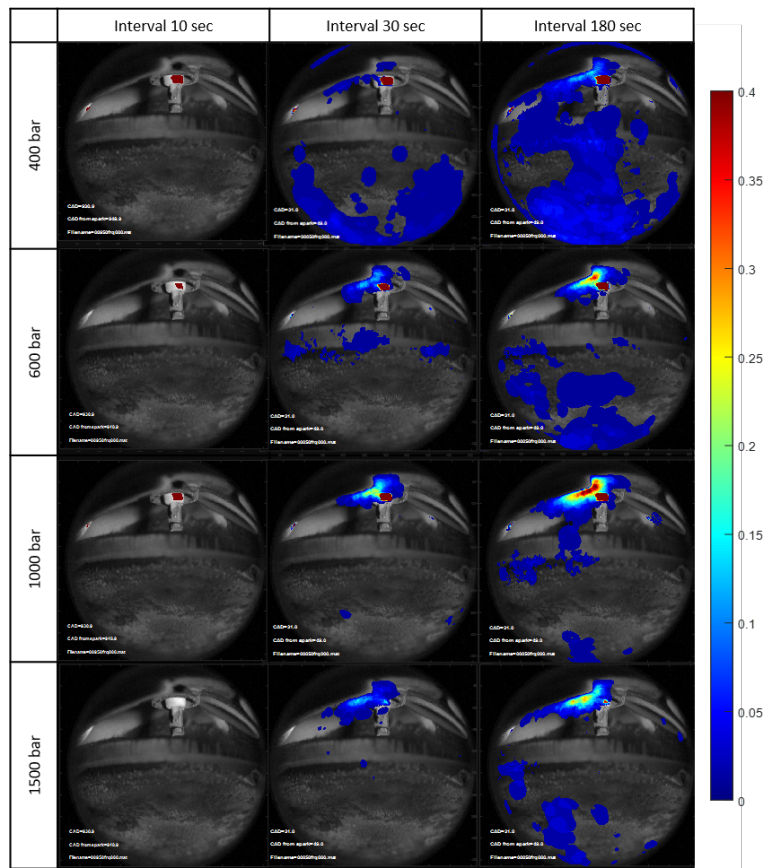


Figure 5.18: Relative frequencies of observation for luminous flames during the first 10 cycles after motoring for various motoring durations and injection pressures under simplified transient conditions



# Chapter 6

## Conclusions and Outlook

The work presented in this thesis focused on the potential for using ultra-high pressure fuel injections to reduce particulate number emissions from gasoline direct injection engines. To this end, the properties of ultra-high pressure sprays and their effects on air flow in the cylinder were characterized experimentally and their impact on combustion characteristics and emissions was determined. This section describes the key findings of the experimental studies and provides answers to the research questions posed in the Introduction.

The first research question pertained to the possible saturation of the beneficial effects ultra-high fuel injection pressures. Measurements of the particle size in sprays formed at different injection pressures revealed an inflection point at around 600 bar; while the droplet size generally decreased as the injection pressure increased, this trend became much less pronounced above the inflection point. As a result, only modest reductions in particle size were seen for injection pressures above 800 bar. It should be noted that this trend was only observed for  $D_{32}$ , which is a representative particle size in the spray;  $Dv_{90}$ , which measures the size of the largest particles in the spray, exhibited a clear decreasing trend even for injection pressures above 1000 bar. Thus, while the reduction in mean particle size upon increasing the fuel pressure does seem to be subject to a saturation effect, the same is not true for the removal of coarse particles. In addition, studies on the spray-induced air flow showed that the intensity of the induced air flow increases with the injection pressure up to 1000 bar. When the fuel pressure is raised to 1500 bar, instantaneous strong flows are still generated but the injection duration becomes so short that the injection ends before the air flow field is fully developed. Based on these experiments, the saturation point for the beneficial effects of high fuel pressures on spray properties and air flow appears to be between 600 bar and 1000 bar. However, subsequent engine tests showed that particulate emissions decreased as the injection pressure increased and this trend persisted even up to injection pressures of 1500 bar when using particularly advanced or retarded SOI timings, although the effect was comparatively small when the SOI timing was 300 °bTDC. We can thus expect injection pressures as high as 1500 bar to have at least some beneficial effects on combustion and emissions.

It is also important to recognize that several factors affect PN emissions, including atomization, wall film formation, and turbulence. However, it is not clear which of these factors has the greatest impact under any particular set of conditions. The experiments presented herein showed that ultra-high injection pressures have beneficial effects on all three factors, but the dominant factor (and thus the overall impact of an ultra-high injection pressure) depends on the injection timing and the environment in the cylinder. For example, at SOI timings that lead to wall film formation (340-310 °bTDC), ultra-high fuel pressures reduce PN emissions because they favor the formation of thinner and wider wall films that evaporate rapidly [27, 53, 55]. Ultra-high fuel pressures also had a significant beneficial impact when using retarded injection timings, which was attributed to accelerated evaporation resulting from improved atomization and accelerated mixture formation due to increased turbulence.

Aside from the beneficial effects on PN emissions discussed above, the use of ultra-high injection pressures was found to have the following positive effects:

- Shorter injection durations
- Better atomization
- More air entrainment and greater air motion
- Better combustion stability
- Reduced HC emissions
- More flexible SOI timing
- Minimized HC and PN emissions from wall films
- Minimization of yellow film formation under transient conditions

Despite these beneficial effects on spray characteristics and emissions, the experiments did not indicate that ultra-high injection pressures had any positive effect on fuel consumption and carbon dioxide emissions. Therefore, it will be necessary to combine high injection pressures with other technologies such as hybrid powertrains to achieve fuel efficiency gains while also reducing PN emissions. In addition, some possible negative effects of ultra-high injection pressures were identified:

- Increased fuel pump work leading to higher fuel consumption
- Increased emissions of fine particulates, which are associated with respiratory disease [18]
- Need for a potentially expensive high pressure fuel system
- Ultra-high pressures may not be available under cold start conditions, which would cause high PN and HC emissions

In addition to these considerations, some obstacles remain to be overcome before ultra-high injection pressures can be used in production engines. First, their beneficial effects must be demonstrated in engine tests in realistic environments. In this work, steady-state hot conditions and different temperature environments were simulated. However, it is necessary to prove that the beneficial effects of ultra-high pressures can be fully realized during real-world driving cycles including cold starts and acceleration transients.

In addition, there is a concern that the energy required to generate ultra-high fuel pressures will reduce fuel efficiency, so the energy ratio of the fuel pump drive may become large under operating conditions such as starts and during low load operation. It will therefore be necessary to find more efficient ways of generating high pressures or to combine the system with a complementary technology such as a hybrid powertrain.

The biggest problem might be the cost, which will inevitably be higher than for a conventional injection system because it is essential to ensure pressure resistance and the ability to establish and control ultra-high pressures. Even if ultra-high pressure sprays can significantly reduce emissions under diverse operating conditions, they may be difficult to use in practice if introducing the requisite systems into GDI engines leads to severe cost increases and changes in specifications. Therefore, further hardware research and development is needed in the area of ultra-high pressure fuel systems.

Although the recent shift to electric vehicles may limit the amount of resources allocated to the development of internal combustion engines, the potential benefits of GDI engines using ultra-high pressures warrant further investigation to ensure that society has the widest possible range of options for future propulsion systems.



# Bibliography

- [1] Richard W. Atkinson et al. “Urban Ambient Particle Metrics and Health”. In: *Epidemiology* 21 (2010), pp. 501–511. DOI: 10.1097/EDE.0b013e3181debc88.
- [2] Tawfik Badawy et al. “Investigation of injector coking effects on spray characteristic and engine performance in gasoline direct injection engines”. In: *Applied Energy* 220 (2018), pp. 375–394. DOI: 10.1016/j.apenergy.2018.03.133.
- [3] Carsten Baumgarten. *Mixture Formation in Internal Combustion Engines*. Reading, Massachusetts: Springer-Verlage Berlin Heidelberg, 2006. ISBN: 9783540308362.
- [4] Alex Berndorfer et al. “Diffusion Combustion Phenomena in GDi Engines caused by Injection Process”. In: *SAE Technical paper* (2013). DOI: 10.4271/2013-01-0261.
- [5] Markus Bertsch. “Experimental Investigations on Particle Number Emissions from GDI Engines”. In: *Ph.D. thesis* (2016). DOI: 10.5445/ir/1000063994.
- [6] Henning Bockhorn. *Soot Formation in Combustion: Mechanisms and Models*. Springer, 1994. ISBN: 9783642851674.
- [7] H. Böhm et al. “The influence of pressure and temperature on soot formation in premixed flames”. In: *Symposium on Combustion* 22 (1989), pp. 403–411. DOI: 10.1016/S0082-0784(89)80047-5.
- [8] Borgwarner. *Fuel injection systems*. <https://www.borgwarner.com/technologies/fuel-injection-systems>.
- [9] S Buri, H Kubach, and U Spicher. “Effects of increased injection pressures of up to 1000 bar - Opportunities in stratified operation in a direct-injection spark-ignition engine”. In: *International Journal of Engine Research* 11 (2010), pp. 473–484. DOI: 10.1243/14680874JER608.
- [10] Gilbert Cadelis, Rachel Tourres, and Jack Molinie. “Short-Term Effects of the Particulate Pollutants Contained in Saharan Dust on the Visits of Children to the Emergency Department due to Asthmatic Conditions in Guadeloupe (French Archipelago of the Caribbean)”. In: *PLoS ONE* 9 (2014), e91136. DOI: 10.1371/journal.pone.0091136.
- [11] A. W. Correia et al. “Effect of air pollution control on life expectancy in the United States: An analysis of 545 U.S. Counties for the period from 2000 to 2007”. In: *Epidemiology* 24 (2013), pp. 23–31. DOI: 10.1097/EDE.0b013e3182770237.

- [12] Ramin Dastanpour and Steven N. Rogak. “Observations of a Correlation Between Primary Particle and Aggregate Size for Soot Particles”. In: *Aerosol Science and Technology* 48 (2014), pp. 1043–1049. DOI: 10.1080/02786826.2014.955565.
- [13] Delphi Technologies. *Worldwide emissions standards: Passenger cars and light duty vehicles 2020/21*. <https://www.delphi.com/sites/default/files/2020-04/DELPHI%20booklet%20emission%20passenger%20cars%202020%20online%20complet.pdf>.
- [14] DENSO CORPORATION. *MAZDA SKYACTIV-D Engine (EURO 6), Common Rail System (CRS) Service Manual*.
- [15] Haichun Ding et al. “The Impact of GDI Injector Deposits on Engine Combustion and Emission”. In: *SAE Technical Paper* (2017). DOI: 10.4271/2017-01-2248.
- [16] EEA. *Final energy consumption by sector and fuel in Europe*. 2019. URL: <https://www.eea.europa.eu/data-and-maps/indicators/final-energy-consumption-by-sector-10/assessment>.
- [17] Y. Fang et al. “Air pollution and associated human mortality: The role of air pollutant emissions, climate change and methane concentration increases from the preindustrial period to present”. In: *Atmospheric Chemistry and Physics* 13 (2013), pp. 1377–1394. DOI: 10.5194/acp-13-1377-2013.
- [18] Barouch Giechaskiel, Urbano Manfredi, and Giorgio Martini. “Engine Exhaust Solid Sub-23 nm Particles: I. Literature Survey”. In: *SAE International Journal of Fuels and Lubricants* (2014). DOI: 10.4271/2014-01-2834.
- [19] Taehoon Han et al. “Multiple injection for improving knock, gaseous and particulate matter emissions in direct injection SI engines”. In: *Applied Energy* 262 (2020), p. 114578. DOI: 10.1016/j.apenergy.2020.114578.
- [20] Sebastian Henkel et al. “Injector Fouling and Its Impact on Engine Emissions and Spray Characteristics in Gasoline Direct Injection Engines”. In: *SAE Int. J. Fuels Lubr.* 10 (2017). DOI: 10.4271/2017-01-0808.
- [21] Hiroyuki Hiroyasu and Masataka Arai. “Structures of Fuel Sprays in Diesel Engines”. In: *SAE Transactions* 99 (1990), pp. 1050–1061. ISSN: 0096736X,25771531.
- [22] Harry Husted, Timothy D. Spegar, and Joseph Spakowski. “The Effects of GDi Fuel Pressure on Fuel Economy”. In: *SAE Technical paper* (2014). DOI: 10.4271/2014-01-1438.
- [23] ICCT. *CO2 emission standards for passenger cars and light-commercial vehicles in the European Union*. 2019. URL: <https://theicct.org/publications/ldv-co2-stds-eu-2030-update-jan2019>.
- [24] IEA. *IEA World Energy Balances 2019*. 2019. URL: <https://webstore.iea.org/world-energy-balances-2019>.

- [25] Yoshihiro Imaoka et al. “A Study of Particulate Emission Formation Mechanism from Injector Tip in Direct-Injection Gasoline Engines”. In: *SAE Int. J. Advances Curr. Prac. in Mobility* 2 (2019), pp. 376–384. DOI: 10.4271/2019-01-2244.
- [26] Changzhao Jiang et al. “Effect of fuel injector deposit on spray characteristics, gaseous emissions and particulate matter in a gasoline direct injection engine”. In: *Applied Energy* 203 (2017), pp. 390–402. DOI: 10.1016/j.apenergy.2017.06.020.
- [27] Niklas Jüngst and Sebastian Kaiser. “Imaging of Fuel-Film Evaporation and Combustion in a Direct-Injection Model Experiment”. In: *SAE Technical paper* (2019). DOI: 10.4271/2019-01-0293.
- [28] Takashi Kaminaga et al. “A Study of Combustion Characteristics of a High Compression Ratio SI Engine with High Pressure Gasoline Injection”. In: *SAE Technical Paper* (2019). DOI: 10.4271/2019-24-0106.
- [29] Ki-Hyun Kim, Ehsanul Kabir, and Shamin Kabir. “A review on the human health impact of airborne particulate matter”. In: *Environment International* 74 (2015), pp. 136–143. DOI: 10.1016/j.envint.2014.10.005.
- [30] Vincent Knop and Eddie Essayem. “Comparison of PFI and DI Operation in a Downsized Gasoline Engine”. In: *SAE Int. J. Engines* 6 (2013), pp. 941–952. DOI: 10.4271/2013-01-1103.
- [31] Tobias Knorsch et al. “On the Evaluation Methods for Systematic Further Development of Direct-Injection Nozzles”. In: *SAE Technical Paper* (2016). DOI: 10.4271/2016-01-2200.
- [32] Felix Leach et al. “A Review of the Requirements for Injection Systems and the Effects of Fuel Quality on Particulate Emissions from GDI Engines”. In: *SAE Technical paper* (2018). DOI: 10.4271/2018-01-1710.
- [33] Z Lee and S Park. “Particulate and gaseous emissions from a direct-injection spark ignition engine fueled with bioethanol and gasoline blends at ultra-high injection pressure”. In: *Renewable Energy* 149 (2020), pp. 80–90. DOI: 10.1016/j.renene.2019.12.050.
- [34] Arthure H Lefebvre. *Atomization and Sprays*. CRC Press, 1989. ISBN: 9780891166030.
- [35] Arthure H Lefebvre and Vincent G McDonell. *Atomization and Sprays, Second Edition*. CRC Press, 2017. ISBN: 9781498736268.
- [36] Bestian Lehnert, Chris Conrad, and Michael Wensing. “GDI Sprays with up to 200 MPa Fuel Pressure and Comparison of Diesel-like and Gasoline-Like Injector Designs”. In: *SAE Technical Paper* (2020). DOI: 10.4271/2020-01-2104.
- [37] LMC Automotive. *Electrification - Global Hybrid Electric Vehicle Forecast*. <https://lmc-auto.com/wp-content/uploads/2019/01/LMC-Electrification-Presentation-January-2019.pdf>.

- [38] Mario Medina, Mohammad Fatouraie, and Margaret Wooldridge. “High-Speed Imaging Studies of Gasoline Fuel Sprays at Fuel Injection Pressures from 300 to 1500 bar”. In: *SAE Technical Paper* (2018). DOI: 10.4271/2018-01-0294.
- [39] K. Meister, C. Johansson, and B. Forsberg. “Estimated short-term effects of coarse particles on daily mortality in Stockholm, Sweden”. In: *Environmental Health Perspectives* 120 (2012), pp. 431–436. DOI: 10.1289/ehp.1103995.
- [40] A Melling. “Trace particles and seeding for particule image velocimetry”. In: *Measurement Science and Technology* 8 (1997), pp. 1406–1416.
- [41] Marianna Migliaccio et al. “Experimental and numerical analysis of a high-pressure outwardly opening hollow cone spray injector for automotive engines”. In: *Fuel* 196 (2017), pp. 508–519. DOI: 10.1016/j.fuel.2017.01.020.
- [42] Alessandro Montanaro, Luigi Allocca, and Giovanni Meccariello. “Effects of Ultra-High Injection Pressures up to 100 MPa on Gasoline Spray Morphology”. In: *SAE Technical Paper* (2020). DOI: 10.4271/2020-01-0320.
- [43] Wolfgang V Ohnesorge. “Die Bildung von Tropfen an Düsen und die Auflösung flüssiger Strahlen”. In: *ZAMM - Journal of Applied Mathematics and Mechanics* 16 (1936), pp. 355–358. DOI: 10.1002/zamm.19360160611.
- [44] Thomas Pauer et al. “New Generation Bosch Gasoline Direct-injection Systems”. In: *MTZ worldwide* 8078 (2017), pp. 16–23. DOI: 10.1007/s38313-017-0053-6.
- [45] Thomas Pauer et al. “New Generation Bosch Gasoline Direct-injection Systems”. In: *MTZ worldwide* 78 (2017), pp. 16–23. DOI: 10.1007/s38313-017-0053-6.
- [46] Raul Payri et al. “Hydraulic Behavior and Spray Characteristics of a Common Rail Diesel Injection System Using Gasoline Fuel”. In: *SAE Technical Paper* (2012). DOI: 10.4271/2012-01-0458.
- [47] Johann Peer et al. “Development of a High Turbulence, Low Particle Number, High Injection Pressure Gasoline Direct Injection Combustion System”. In: *SAE International Journal of Engines* 9 (2016), pp. 2301–2311. DOI: 10.4271/2016-01-9046.
- [48] Jonathan James Pilbean et al. “Study of Effects of Deposit Formation on Di Injector and Engine Performance”. In: *SAE Technical Paper* (2020). DOI: 10.4271/2020-01-2099.
- [49] Walter F Piock et al. “Fuel Pressure and Charge Motion Effects on GDi Engine Particulate Emissions”. In: *SAE International Journal of Engines* 8 (2015), pp. 464–473. DOI: 10.4271/2015-01-0746.
- [50] Lucio Postriotti et al. “Experimental and Numerical Analysis of Spray Evolution, Hydraulics and Atomization for a 60 MPa Injection Pressure GDI System”. In: *SAE Technical Paper* (2018). DOI: 10.4271/2018-01-0271.
- [51] C Preussner et al. “GDI: Interaction Between Mixture Preparation, Combustion System and Injector Performance”. In: *SAE Technical Paper* (1998). DOI: 10.4271/980498.



- [52] Vincenzo Rossi, Nicola Silvestri, and Massimo Medda. “Experimental Investigations on Engine-Out Emissions Sensitivity to Fuel Injection Pressure of a High-Performance DISI Single Cylinder Engine”. In: *SAE Technical Paper* (2019). DOI: 10.4271/2019-24-0169.
- [53] Soichi Saitoh et al. “Evelution of Gasoline Direct Injection System for Reduction of Real Mode Emission”. In: *SAE Technical paper* (2019). DOI: 10.4271/2019-01-0265.
- [54] Georges Saliba et al. “Comparison of Gasoline Direct-Injection (GDI) and Port Fuel Injection (PFI) Vehicle Emissions: Emission Certification Standards, Cold-Start, Secondary Organic Aerosol Formation Potential, and Potential Climate Impacts”. In: *Environmental Science and Technology* 51 (2017), pp. 6542–6552.
- [55] F. Schulz and F. Beyrau. “The effect of operating parameters on the formation of fuel wall films as a basis for the reduction of engine particulate emissions”. In: *Fuel* 238 (2019), pp. 375–384. DOI: 10.1016/j.fuel.2018.10.109.
- [56] Jaeheon Sim, Jihad A Badra, and Hong G Im. “Hollow-Cone Spray Modeling for Opeing Piezoelectric Injector”. In: *54th AIAA Aerospace Sciences Meeting* (2016).
- [57] Jingeun Song et al. “Effects of injection strategy and coolant temperature on hydrocarbon and particulate emissions from a gasoline direct injection engine with high pressure injection up to 50MPa”. In: *Energy* 164 (2018), pp. 512–522. DOI: 10.1016/j.energy.2018.09.011.
- [58] Andreas Stadler et al. “Experimental Investigations on High Pressure Gasoline Injection up to 800 bar for Different Combustion Modes”. In: *MTZ worldwide* 80 (2019), pp. 52–57. DOI: 10.1007/s38313-018-0161-y.
- [59] J Stegeman et al. “Influence of throttle effects at the needle seat on the spray characteristics of a multihole injection nozzle”. In: *ILASS-Europe* (2002).
- [60] Jianye Su et al. “Particle Number Emissions Reduction Using Multiple Injection Strategies in a Boosted Spark-Ignition Direct-Injection (SIDI) Gasoline Engine”. In: *SAE Int. J. Engines* 8 (2015). DOI: 10.4271/2014-01-2845.
- [61] Takeshi Ueki. “Research on the reduction of particulate matter in gasoline direct injection engines (Translated from Japanese.)” In: *Ph.D. thesis* (2018). DOI: 10.14988/di.2018.0000000327.
- [62] Yuan Wen et al. “The Impact of Injector Deposits on Spray and Particulate Emission of Advanced Gasoline Direct INjection Vehicle”. In: *SAE Technical Paper* (2016). DOI: 10.4271/2016-01-2284.
- [63] Paul Whitaker et al. “Measures to Reduce Particulate Emissions from Gasoline DI engines”. In: *SAE Int. J. Engines* 4 (2011), pp. 1498–1512. DOI: 10.4271/2011-01-1219.
- [64] M Wirth et al. “The Next Generation of Gasoline Direct Injection: Improved Fuel Economy and Optimizaed System Cost”. In: *Advanced engine design performance* (2003), pp. 139–152.

- 
- [65] Akichika Yamaguchi et al. “Air Motion Induced by Ultra-High Injection Pressure Sprays for Gasoline Direct Injection Engines”. In: *SAE Int. J. Fuels Lubr.* (2020). DOI: 10.4271/04-13-03-0014.
- [66] Akichika Yamaguchi et al. “Spray Characterization of Gasoline Direct Injection Sprays Under Fuel Injection Pressures up to 150 MPa with Different Nozzle Geometries”. In: *SAE Technical paper* (2019). DOI: 10.4271/2019-01-0063.
- [67] F. Zhao, M.C. Lai, and D.L. Harrington. “Automotive spark-ignited direct-injection gasoline engines”. In: *Progress in Energy and Combustion Science* 25 (1999), pp. 437–562. DOI: 10.1016/S0360-1285(99)00004-0.

**Part II**  
**Appended Papers**

